

Analog fast Fourier transforms for scalable and efficient signal processing

T. Patrick Xiao^{1*}, Ben Feinberg¹, David K. Richardson¹, Matthew Cannon¹,
Harsha Medu², Vineet Agrawal², Matthew J. Marinella³, Sapan Agarwal⁴,
Christopher H. Bennett^{1*}

^{1*}Sandia National Laboratories, Albuquerque, 87123, New Mexico, USA.

²Infineon Technologies, San Jose, 95134, California, USA.

³Department of Electrical, Computer, and Energy Engineering, Arizona State University,
Tempe, 85281, Arizona, USA.

⁴Sandia National Laboratories, Livermore, 94551, California, USA.

*Corresponding author(s). E-mail(s): txiao@sandia.gov; cbennet@sandia.gov;
Contributing authors: bfeinbe@sandia.gov; dkricha@sandia.gov; mcannon@sandia.gov;
Harsha.Medu@infineon.com; Vineet.Agrawal@infineon.com; m@asu.edu;
sagarwa@sandia.gov;

Abstract

Edge devices are being deployed at increasing volumes to sense and act on information from the physical world. The discrete Fourier transform (DFT) is often necessary to make this sensed data suitable for further processing – such as by artificial intelligence (AI) algorithms – and for transmission over communication networks. Analog in-memory computing has been shown to be a fast and energy-efficient solution for processing edge AI workloads, but not for Fourier transforms. This is because of the existence of the fast Fourier transform (FFT) algorithm, which enormously reduces the complexity of the DFT but has so far belonged only to digital processors. Here, we show that the FFT can be mapped to analog in-memory computing systems, enabling them to efficiently scale to arbitrarily large Fourier transforms without requiring large sizes or large numbers of non-volatile memory arrays. We experimentally demonstrate analog FFTs on 1D audio and 2D image signals, using a large-scale charge-trapping memory array with precisely tunable, low-conductance analog states. The scalability of both the new analog FFT approach and the charge-trapping memory device is leveraged to compute a 65,536-point analog DFT, a scale that is otherwise inaccessible by analog systems and which is $>1000\times$ larger than any previous analog DFT demonstration. The analog FFT also provides more numerically precise DFTs with greater tolerance to device and circuit non-idealities than a direct matrix-vector multiplication approach. We show that the extension of the FFT algorithm to analog in-memory processors leads to design considerations that differ markedly from digital implementations, and that analog Fourier transforms have a substantial power efficiency advantage at all size scales over FFTs implemented on state-of-the-art digital hardware.

1. Introduction

The increasing deployment of remote and inter-connected sensors and actuators is leading to the collection of ever larger volumes of data from the physical world. Acting on this information in real time requires computation to be done on the data where it is sensed – at the “edge” of the network – and the raw sensed signals often must be processed by linear transforms to be made suitable for further processing, communication, or storage. One of the most ubiquitous transforms is the discrete Fourier transform (DFT), which converts a spatial or temporal digital signal to its frequency representation. When used in an edge or Internet-of-Things (IoT) device, the DFT can form images of the sensed environment from radar data [1–4], filter and amplify audio signals to aid in hearing [5, 6], and modulate signals for broadband wireless communication with other IoT devices [7–9]. An indispensable instrument for real-time signal processing on power-starved systems is the fast Fourier transform (FFT) algorithm, which reduces the computational complexity of the DFT [10]. Despite the efficiency of this algorithm, the end of Dennard scaling means that there will no longer be improvements to the energy per arithmetic operation using CMOS logic [11]. Therefore, conventional digital processors may soon prove inadequate for the large-scale data processing capabilities that are desired in future edge or IoT devices.

Analog in-memory computing (IMC) systems are a potential solution to overcome these scaling limits. These systems exploit analog circuit laws to rapidly and efficiently compute matrix operations inside non-volatile memory arrays, while greatly reducing the crippling energy overhead of data movement between the memory and processor in traditional von Neumann architectures [12–14]. These advantages enable analog IMC to process machine learning (ML) inference workloads with potentially orders-of-magnitude greater performance per watt, as explored in numerous recent works [15–22]. However, the same benefits have yet to materialize for executing the important DFT operations that often come before or after the ML algorithm in edge systems, and would thus become the bottleneck. This is because while the DFT can be expressed as a matrix-vector multiplication (MVM), it can be computed using far fewer mathematical operations by using the FFT algorithm. While this enormous advantage has been enjoyed by digital processors for decades, analog IMC systems have yet to capitalize on the benefits of the FFT, severely limiting their efficiency and scalability.

Analog IMC systems to date have relied exclusively on a direct MVM mapping of the DFT and its real-only counterpart, the discrete cosine transform (DCT) [23]. With this approach, analog IMC retains its low energy-per-operation only up to DFT sizes that can fit within a single memory array. Therefore, the largest experimentally demonstrated analog DFTs and DCTs are on signals containing only 64 points per dimension [24–26]. Relying on these prior methods would preclude analog processing from scaling to the much larger DFT sizes needed for many practical applications.

In this article, we propose and demonstrate a new, more scalable mapping of the Fourier transform onto analog IMC architectures that is based on the classic Cooley-Tukey FFT algorithm [27]. This method factorizes large DFTs into smaller elementary DFTs that are then computed by analog MVMs, which enables a single modestly sized memory array to efficiently process arbitrarily large DFTs when accompanied by a small amount of digital processing. Compared to prior analog IMC approaches, the analog FFT reduces the energy and area scaling of the DFT from $O(N^2)$ to $O(N\log N)$, just as the original FFT algorithm reduced the complexity of the DFT on digital processors. However, the optimal analog implementation of the FFT has essential differences from the optimal digital implementation, and achieves its $O(N\log N)$ scaling in a different way. Along with higher efficiency, the analog FFT can also yield more accurate DFTs than prior analog IMC approaches, independently of the memory technology used for computing.

As a proof-of-concept, we have implemented analog FFTs on a large array of charge-trapping flash memory devices based on the silicon-oxide-nitride-oxide-silicon (SONOS) material stack, and experimentally computed the frequency spectra of 1D audio and 2D image signals. The subthreshold operation and precise analog programmability of this memory enables half a million devices to simultaneously participate in a single analog MVM while retaining high accuracy. Leveraging the scalability of both the FFT and the SONOS memory technology, we compute analog DFTs of up to 65,536 points, three orders of magnitude larger than any prior DFT computed using analog hardware. We also show that while the energy of both analog and digital FFTs fundamentally scales as $O(N\log N)$, analog FFTs can have a $15\times$ to $60\times$ energy advantage at all practical DFT sizes over digital FFTs. This is benchmarked by simulating 40-nm node SONOS analog IMC circuits and by executing FFT designs on the 7-nm node AMD Xilinx Versal chip, which contains dedicated accelerators for signal processing. Our results demonstrate the versatility of analog accelerators to reach the scale and accuracy needed for practical workloads, not just in ML but across a wide range of signal processing applications.

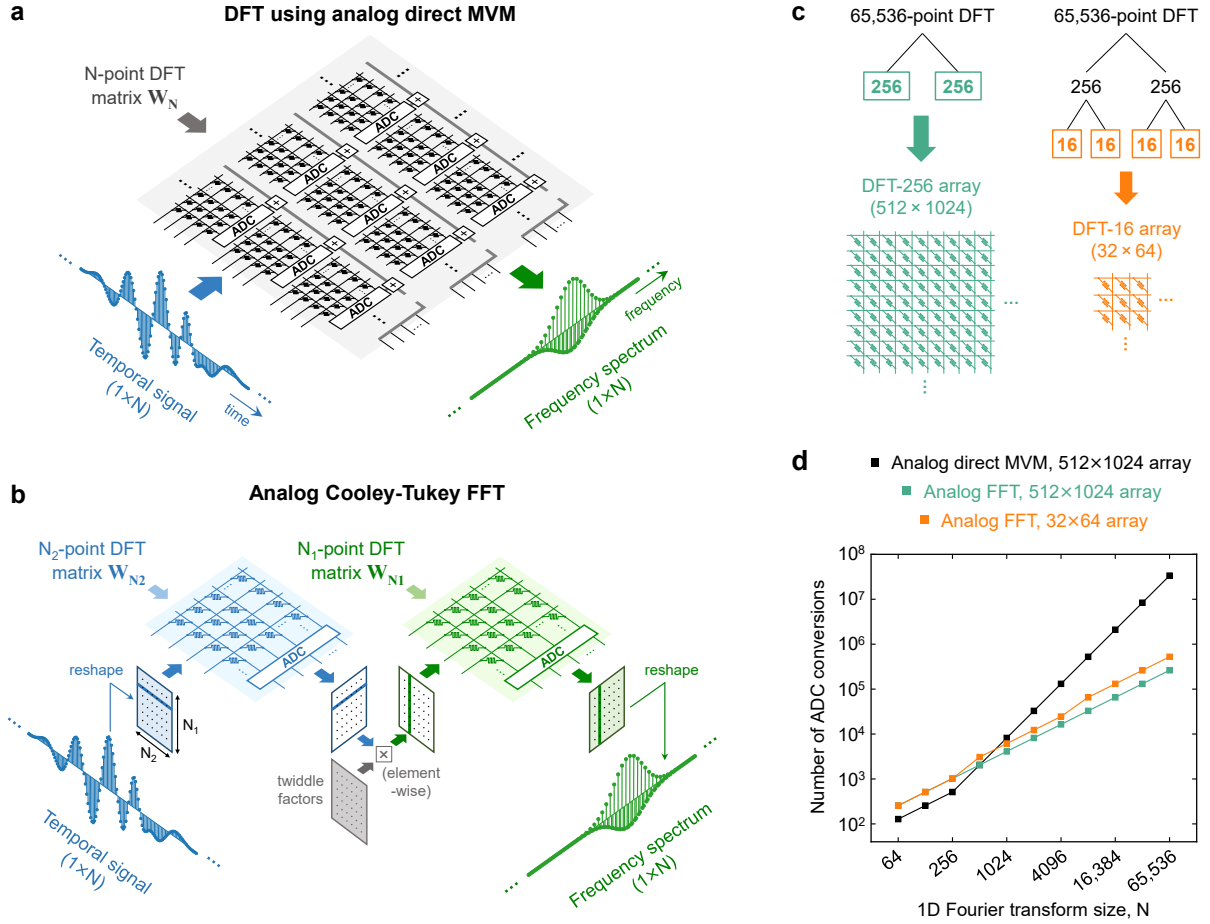


Fig. 1 Processing large discrete Fourier transforms using analog in-memory computing. (a) The analog direct MVM approach to computing the DFT requires a large DFT matrix to be split across many arrays. (b) The analog Cooley-Tukey FFT factorizes the N -point DFT into smaller DFTs of size N_1 and N_2 . Only the real part of the temporal signal and frequency spectrum are shown for simplicity. (c) Two of many possible ways to factorize a 65,536-point DFT using the analog FFT. The leaves of the trees are elementary DFTs mapped to analog MVMs, and the branches are Cooley-Tukey factorizations. (d) Comparison of how the number of ADC conversions scales with DFT size, for the analog direct MVM and the analog FFT. We consider analog IMC systems with a maximum single-array DFT size of 256 points (512×1024 array size), and 16 points (32×64 array size).

2. The analog fast Fourier transform

Analog in-memory computing systems and digital processors are governed by fundamentally different scaling laws for their energy consumption. The energy associated with digital processing generally scales with the number of arithmetic operations such as multiplies and adds. Analog IMC systems follow a different scaling law, due to an essential characteristic of these architectures: though the matrix computations inside the memory array are extremely efficient, almost all the energy is consumed by peripheral circuits, particularly those involved in sensing and converting analog summed currents to digital outputs of 8-bit or higher resolution [13, 18, 28–30]. Therefore, the total required number of conversions by the analog-to-digital converter (ADC) is a useful measure that is expected to scale together with the total energy consumption, independent of the specific memory technology or circuit implementation.

Beyond its importance for signal processing, the discrete Fourier transform epitomizes the different ways that the two hardware paradigms can scale. The DFT converts a one-dimensional signal \mathbf{x} with length N to its frequency spectrum \mathbf{X} :

$$X_k = \sum_{n=0}^{N-1} x_n e^{-i2\pi nk/N} \quad (1)$$

This equation can be explicitly written as a complex-valued MVM: $\mathbf{X} = \mathbf{W}_N \mathbf{x}$, where \mathbf{W}_N is the DFT matrix of size $N \times N$. The element at the (n, k) position of this matrix has the value $(\omega_N)^{nk}$, where $\omega_N = e^{-i2\pi/N}$.

In digital hardware, the DFT is generally computed using an FFT algorithm. The FFT exploits divide-and-conquer techniques to compute the DFT using far fewer operations than by computing the above MVM directly. This fundamentally reduces the DFT’s computational complexity, and hence its energy scaling, from $\mathcal{O}(N^2)$ to $\mathcal{O}(N \log_2 N)$ [10]. The reduction is possible by exploiting the symmetries of the DFT matrix. For matrices without symmetry or periodicity, such as matrices of deep neural network (DNN) weights, the number of operations is irreducible without the use of approximations.

The conventional analog IMC approach to the DFT is to first expand the matrix \mathbf{W}_N into its real and imaginary parts, program the resulting matrix onto a resistive memory crossbar, then compute the DFT directly as an analog MVM [23, 24, 26, 31]. When the DFT is computed directly using a single array, the energy scales simply with the number of outputs of a DFT; that is, $\mathcal{O}(N)$. However, this result holds only for small N . As N becomes large, the matrix \mathbf{W}_N eventually exceeds the maximum size of a memory array. The upper bound on the physical array size can arise from many factors, including the maximum current supported by the peripheral circuitry [18], parasitic IR voltage drops along the array interconnects [32], accumulation of memory device conductance errors and noise [33], write disturb due to accumulated leakage currents [34], and process yield considerations. Extending the direct MVM approach to this regime requires a large DFT matrix to be split across many physical arrays, with each array producing partial results that must be digitized then added, as shown in Fig. 1a. In this case, the number of ADC conversions needed to produce a single DFT output scales as $\mathcal{O}(N)$, leading to an overall energy scaling of $\mathcal{O}(N^2)$. The area scales either with the total number of ADCs (if peripheral circuits are larger) or the number of elements in the DFT matrix (if the array is larger); in either case, the area scaling is also $\mathcal{O}(N^2)$. The rapid, quadratic growth of both energy and area with N limits the size and nature of problems that can be processed efficiently with this approach using analog hardware.

We now show that the FFT algorithm can be implemented on analog IMC hardware, with some special considerations, to inherit its fundamental scalability benefits. We specifically use the mixed-radix formulation of the Cooley-Tukey FFT algorithm [10], considering a DFT size that is a composite number $N = N_1 \times N_2$. The input \mathbf{x} and output \mathbf{X} , which are vectors of length N , can be reshaped into matrices with dimensions $N_1 \times N_2$: we call these $\tilde{\mathbf{x}}$ and $\tilde{\mathbf{X}}$, respectively. The indices of the new matrices are related to those of the original vectors by: $\tilde{x}_{n_1, n_2} = x_{n_1 + N_1 n_2}$ and $\tilde{X}_{k_1, k_2} = X_{N_2 k_1 + k_2}$. By exploiting the periodicity of \mathbf{W}_N , Equation 1 can be re-written as:

$$\tilde{X}_{k_1, k_2} = \sum_{n_1=0}^{N_1-1} \omega_{N_1}^{n_1 k_1} \omega_N^{n_1 k_2} \sum_{n_2=0}^{N_2-1} \omega_{N_2}^{n_2 k_2} \tilde{x}_{n_1, n_2} \quad (2)$$

To explicitly show the mapping onto analog hardware, this equation can be cast in matrix form as:

$$\tilde{\mathbf{X}} = \mathbf{W}_{N_1} [\mathbf{T} \odot (\mathbf{W}_{N_2} \tilde{\mathbf{x}})] \quad (3)$$

where \odot denotes the element-wise (or Hadamard) product and \mathbf{T} is an $N_1 \times N_2$ matrix of twiddle factors defined by $\mathbf{T}_{mn} = (\omega_N)^{mn}$. Fig. 1b shows the sequence of steps that implement the analog FFT in Equation 3. The input vector \mathbf{x} is initially reshaped into the matrix $\tilde{\mathbf{x}}$. In the first stage, an N_2 -point DFT is computed for every row of the matrix $\tilde{\mathbf{x}}$ using a sequence of analog MVMs on a resistive memory array; this executes the matrix-matrix multiplication $\mathbf{W}_{N_2} \tilde{\mathbf{x}}$. The results are digitized and multiplied element-wise with the twiddle matrix \mathbf{T} using digital multipliers. Next, a second stage of N_1 -point DFTs is executed to perform the multiplication with \mathbf{W}_{N_1} , again via a sequence of analog MVMs. Finally, the result $\tilde{\mathbf{X}}$ is reshaped back into a vector to obtain \mathbf{X} .

The above Cooley-Tukey decomposition enables a large N -point DFT, which otherwise needs to be split across many arrays, to be computed with just two arrays that implement an N_1 -point analog DFT and an N_2 -point analog DFT, respectively. To scale to very large N , or to enable small memory arrays to scale to large N , the Cooley-Tukey factorization can be applied recursively to further reduce the elementary DFT sizes, or radices, as shown in Fig. 1c. The physical size of the memory array sets the upper bound on the size K of an elementary DFT, though a smaller value of K may be chosen to optimize accuracy. To support a K -point elementary analog DFT within a single array, the array needs to have at least $2K$ rows and $4K$ columns [23].

Fig. 1d compares how the number of required ADC conversions scales between the two analog DFT approaches. For the direct MVM method, we assumed an array size ($K = 256$) that corresponds to the largest analog MVM that can be executed by the SONOS array used in this work, and also matches the array size in other large analog IMC demonstrations to date [20]. The array’s dimensions set the critical DFT size where the scaling behavior of the direct MVM method transitions from $\mathcal{O}(N)$ to $\mathcal{O}(N^2)$. For

the analog FFT, we considered both a large array ($K = 256$) and a small array ($K = 16$). If the Cooley-Tukey decomposition is only applied once, i.e. $N \leq K^2$, the total number of ADC conversions in the analog FFT scales as $\mathcal{O}(N)$, as do the number of digital twiddle multiplications and memory accesses. When the DFT is recursively factorized, all of these operations increase proportionally with the number of Cooley-Tukey decompositions, which scales as $\mathcal{O}(\log_K N)$, as explained in more detail in Supplementary Section S5. Combining these two trends, the energy of the analog FFT scales as $\mathcal{O}(N \log_K N)$ in the limit of large N . This is superior to the $\mathcal{O}(N^2)$ scaling of the analog direct MVM approach, leading to orders-of-magnitude lower energy consumption for large DFT sizes.

The overall $\mathcal{O}(N \log N)$ scaling of the analog FFT is similar to that of the digital FFT, but there are essential differences in the algorithmic structure. In digital FFT implementations, recursively decomposing the DFT down to the smallest possible elementary DFTs (i.e. radix-2 or radix-4) optimally reduces the complexity from $\mathcal{O}(N^2)$ to $\mathcal{O}(N \log_2 N)$ [10]. Meanwhile, the need for recursive decomposition increases the energy complexity of the analog FFT from $\mathcal{O}(N)$ to $\mathcal{O}(N \log_K N)$. For analog FFTs, it is more optimal from an energy standpoint to minimize the depth of the Cooley-Tukey factorization tree by terminating the decomposition as soon as the factored DFT is small enough to fit onto one memory array. Further factorization would decrease the total number of arithmetic operations, which is helpful for digital systems, but would increase the number of intermediate DFT results and hence the number of ADC conversions, which is harmful for analog systems. This explains why having a larger physical array size is more energy-efficient for large analog FFTs, as shown in Fig. 1d. Mathematically, because of the $\mathcal{O}(N \log_K N)$ scaling of the analog FFT, increasing the array size (through K) logarithmically reduces the power consumption. This weak scaling with array size means that even small arrays (or small MVMs within large arrays) can scale to large FFTs without a significant energy penalty, but there is still an energy benefit for FFT applications to develop memory arrays that can support large yet accurate analog MVMs.

3. Analog DFTs using SONOS charge-trapping memory

To execute analog FFTs, we used an array of SONOS charge-trapping memory devices that were optimized to have stable and precisely programmable analog conductance levels. The state variable of SONOS memory is the amount of charge that is confined in a silicon nitride charge-trapping layer, which modulates the electronic conductance of the underlying silicon channel through the field effect. A 1024×1024 crossbar array of SONOS devices was fabricated in a 40-nm node CMOS process that uses the compact two-transistor (2T) memory cell shown in Fig. 2a. The array was integrated with peripheral CMOS circuits to support analog MVMs and write-verify programming of each SONOS device to a target conductance. To minimize conductance change over time, the programming procedure selectively places charge in mid-gap electronic traps in the nitride layer that have large energy barriers for escape, as has been described elsewhere [35–37].

The analog DFT mapping in Fig. 2b is used to multiply a complex-valued DFT weight matrix with a complex-valued vector [23]. The difference in conductance of two SONOS devices encodes the signed value of each real or imaginary weight. To execute a DFT, the input vector \mathbf{x} is applied bit-serially to the select gate lines, and each selected SONOS cell draws a current from its bit line (BL) that is proportional to its conductance. Each BL’s voltage is held at 0.06V, and the analog sum of currents collected on the BL is converted to a voltage by a transimpedance amplifier (TIA), then to digital outputs using an ADC [37]. Digital post-processing accumulates the analog MVM results for different input bits and produces the complex-valued DFT output \mathbf{X} . The ADC has a resolution of 12 bits over the range from 0 to 17 μA .

Prior to programming the DFT matrices, we statistically characterized the programming precision and device-to-device variations of the SONOS memory states across 128 target conductance levels, shown in Fig. 2c (see Methods for details). Over the utilized conductance range from 0 to 24 μS , the variability in conductance is less than 0.4 μS just after programming, and remains below 0.6 μS when measured after three days. Because the SONOS channel is operated in the subthreshold region, the device has a large conductance On/Off ratio ($>10^6$) with errors that approach zero in the low conductance limit [36].

Fig. 2d and Fig. 2e show the measured conductance profiles of a portion of the SONOS array after programming a DFT-16 matrix (2048 devices) and a DFT-256 matrix (524,288 devices), respectively. A maximum target SONOS conductance of 20 μS was used for the DFT-16 subarray, while the DFT-256 subarray used a reduced maximum conductance of 6.2 μS to ensure that the summed currents in our audio processing experiments do not exceed the ADC’s limits. Fig. 2f shows the locations in the complex plane of the DFT weights that were programmed into the SONOS array, whose ideal values ($e^{i2\pi nk/K}$) would lie perfectly along the unit circle. The SONOS-encoded DFT weights are tightly distributed around the circle, with a mean absolute error of $\epsilon_{|\omega|} = 0.0118$ in magnitude and $\epsilon_{\angle\omega} = 0.0059$ radians (0.338°) in

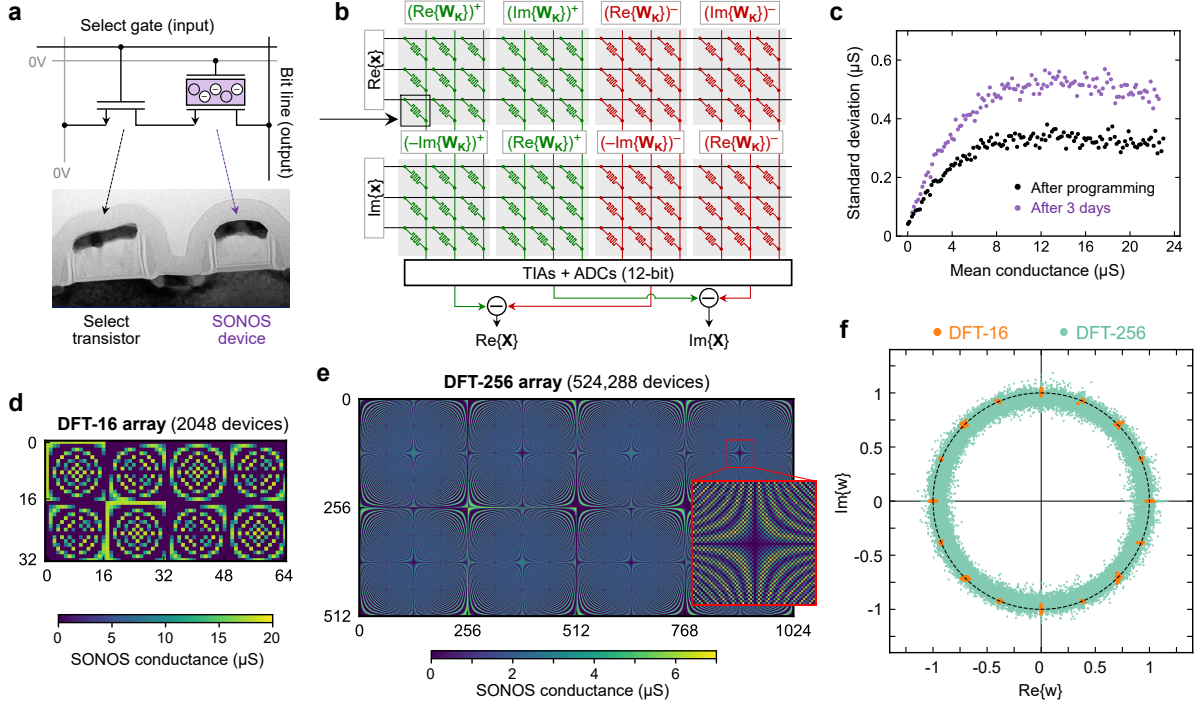


Fig. 2 Mapping a DFT onto a SONOS charge-trapping memory array. (a) Electrical schematic (top) and scanning electron microscope image (bottom) of the two-transistor SONOS memory cell. (b) Mapping a DFT to a resistive memory crossbar, including the spatial layout of complex-valued weights and inputs. The SONOS cell with the input-output connections in (a) is simplified in this schematic to a resistor. (c) Conductance precision vs state for the SONOS cells, accounting for device-to-device variations and drift. Each point represents the statistics of 512 devices programmed to the same target. (d) Measured SONOS conductance profile for a DFT-16 matrix. (e) Measured SONOS conductance profile for a DFT-256 matrix. Inset shows a 64×64 region of the programmed array. (f) Constellation of the complex-valued DFT weight values stored in the programmed SONOS devices, for DFT-16 (orange) and DFT-256 (teal). The ideal DFT weights lie along the unit circle (black dashed circle).

phase for the DFT-16 weights. For the DFT-256 weights, the errors are somewhat larger: $\epsilon_{|\omega|} = 0.0458$ and $\epsilon_{\angle\omega} = 0.0181$ radians (1.037°). This is because the smaller conductances used for the larger matrix lead to a smaller ratio between the signal and error components of the conductance. Conductance statistics for DFT arrays of various sizes can be found in Supplementary Section S4. Large DFT matrices have values that are distributed approximately uniformly over the conductance range; this differs dramatically from DNN weight matrices, which generally have an abundance of near-zero weights and are exponentially skewed toward low conductance [33, 36]. This implies that for the same array size, analog DFT operations will accumulate larger currents, and potentially larger errors, than the typical MVM operations used for DNN inference.

4. Audio processing using analog FFTs

To experimentally demonstrate the analog Cooley-Tukey FFT and evaluate its accuracy, we used the SONOS array as a spectrum analyzer for audio waveforms. A useful representation of the spectrum of a signal is the spectrogram, which shows how the signal’s frequency content changes with time [38]. A spectrogram is generated by computing the DFT of temporal sliding windows of the signal, computing the magnitude of each complex-valued spectrum, then stacking the spectra along the time axis. For this experiment, we used a four-second audio waveform from the Flickr8k Audio Caption dataset [39], with slight zero-padding to 65,536 samples (4.096 seconds at 16 kHz sampling rate). The waveform is shown in Fig. 3a and contains the spoken caption, “Two dogs reach for a yellow frisbee as it flies through the air.” Fig. 3b shows the spectrogram of this signal with a window size of 256 samples, computed using 256-point digital FFTs at single-precision floating-point (FP32) on a CPU. Fig. 3c shows the spectrogram generated experimentally using analog FFTs, where each 256-point FFT was decomposed into 16-point DFTs ($N_1 = N_2 = 16$) and computed using the SONOS subarray in Fig. 2d.

The SONOS-computed spectrogram reproduces all of the key features of the FP32 spectrogram and resolves the frequency signature of each spoken word. The peak signal-to-noise ratio (PSNR), which

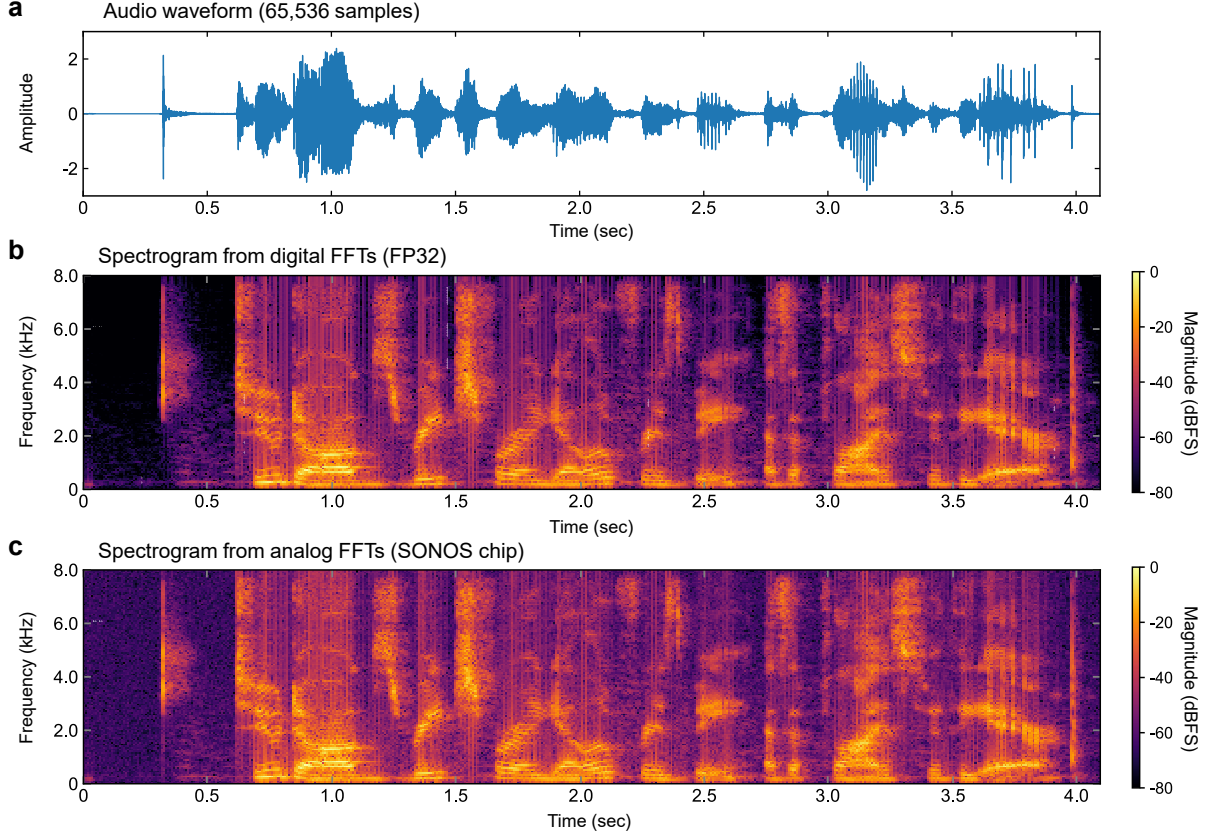


Fig. 3 Spectrogram generation with analog FFTs. (a) Audio waveform with 65,536 samples from the Flickr Audio Caption dataset. (b) Spectrogram of the audio waveform generated by FP32 256-point FFTs, using a window size of 256 samples and a hop length of 128 samples. (c) Same spectrogram generated experimentally using 256-point analog FFTs, factored into 16-point analog DFTs that are executed on the SONOS array. Magnitudes are shown on a logarithmic scale and expressed in dBFS, normalized by the maximum magnitude of the spectrogram in (b).

measures the element-wise error between the two spectrograms, is 41.61 dB. The main visible difference between the spectrograms is the presence of a noise floor in the SONOS spectrogram at around -70 dBFS (decibels relative to full-scale), which originates from device-to-device variability and cycle-to-cycle read noise in the SONOS conductances, accumulated over many devices in an analog MVM. As another assessment of the spectrogram’s quality, we reconstructed the four-second audio waveform by digitally computing the inverse FFT (IFFT) on the SONOS-computed spectrum of each sliding window; both the original and reconstructed audio files are provided as Supplementary Information. Each spoken word is clearly reproduced in the reconstructed audio clips. The noise floor that is present in all frequency bins introduces white noise that can be heard as a faint background static in the reconstructed audio.

To demonstrate the scalability of the analog FFT, we use the SONOS array to compute a 65,536-point FFT, sufficient to generate the spectrum of the full audio waveform in Fig. 3a without breaking it up into sliding windows. The 65,536-point analog FFT is computed by factoring it into 256-point analog DFTs (i.e. $N_1 = N_2 = 256$) that were executed on the SONOS subarray in Fig. 2e. We note that a transform size of 65,536 points is far too large to be feasibly implemented in analog without the Cooley-Tukey FFT; if using a direct MVM approach, the partitioned collection of arrays would need to have 3.4×10^{10} memory devices in total. The magnitude spectrum of the audio waveform as computed experimentally by the SONOS array is shown in Fig. 4a, alongside the true spectrum computed at FP32 precision. The left inset zooms into the frequency range of female human speech (~ 165 to 255 Hz [40]), showing close point-by-point agreement between the SONOS and FP32 computations. Across the full range of frequencies, the SONOS-computed spectrum has a PSNR of 38.16 dB relative to FP32.

To better understand the sources of error in the analog FFT, Fig. 4b shows the error statistics of the current sums (representing dot products) across all analog MVMs used to generate the spectrum in Fig. 4a, and the MVMs used to generate the spectrogram in Fig. 3c. The essential difference between these cases is the size of the elementary analog array operation: the former used 256-point analog DFTs while the latter used 16-point analog DFTs. For small summed currents, the error is random and zero-centered in both cases, and originates from accumulated random variability and noise in the conductances of the

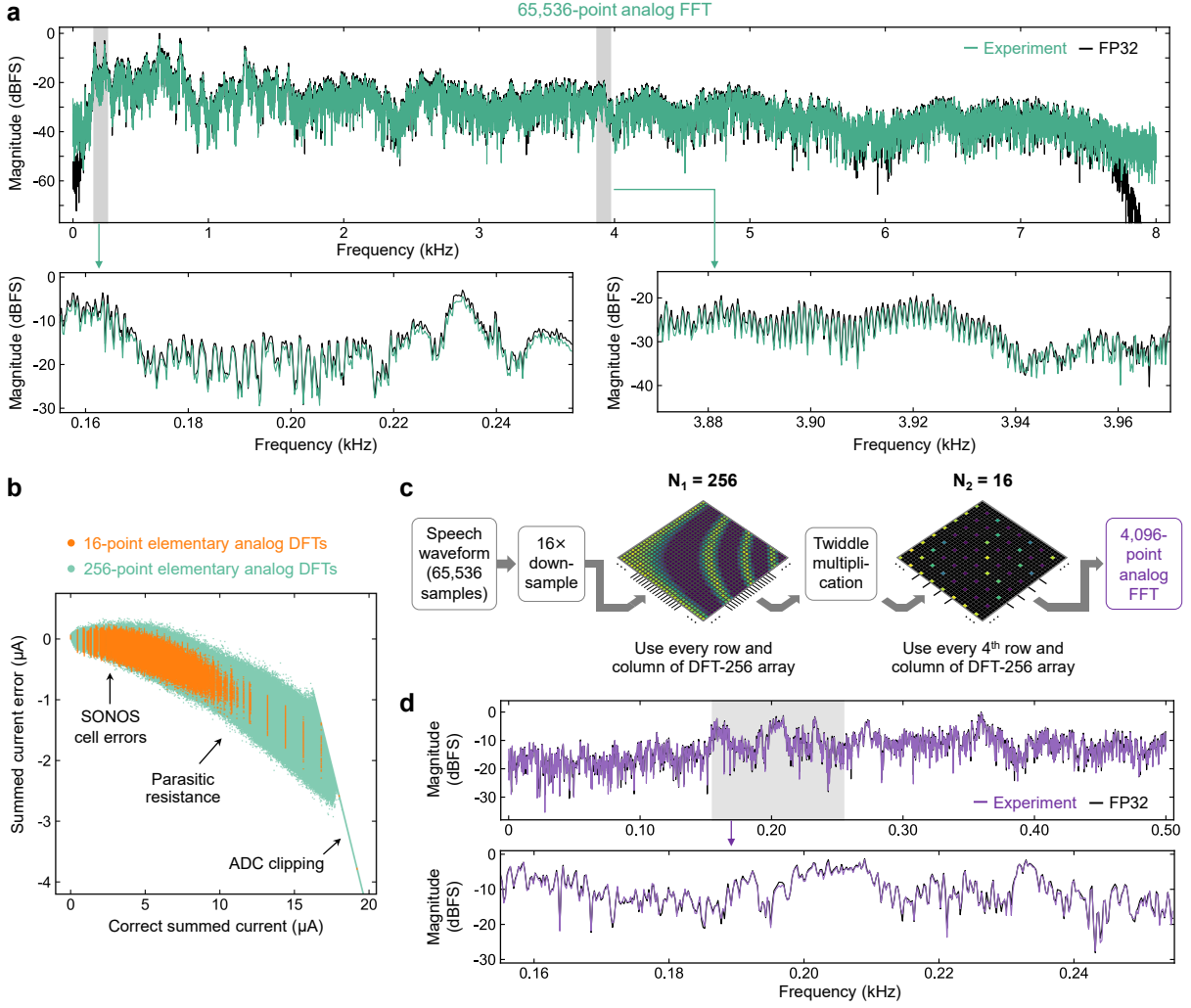


Fig. 4 Demonstration of large-scale, reconfigurable analog FFTs. (a) Magnitude spectrum computed by a 65,536-point analog FFT using the SONOS array (teal) for the full audio signal in Fig. 3a, compared to an FP32 digital FFT (black). The analog FFT was factored into 256-point analog DFTs. Insets zoom in on two parts of the spectrum, including the 165–255 Hz range for female human speech. The frequency resolution is 0.244 Hz. (b) Accuracy of individual analog MVMs, showing how the error in the summed currents depends on the correct value of the analog sum. Teal points (12.6M in total) correspond to the FFT in (a). Orange points (25.1M in total) are currents involved in the spectrogram computation in Fig. 3c, using 16-point analog DFTs. (c) The FFT size can be dynamically reconfigured without re-programming any devices. As an example, we can selectively activate the rows and columns of the 256-point DFT subarray to implement a 16-point DFT. Images show a 32×32 portion of the DFT-256 array; unused devices are colored black. (d) SONOS-computed magnitude spectrum of the 4,096-point down-sampled audio signal (top), and a zoom into one portion of the spectrum (bottom).

SONOS devices as mentioned before. At intermediate to large summed currents, the error is dominated by parasitic IR drops across the resistances of the array’s rows and columns, which causes a systematic reduction in current [32]. This ultimately causes high-valued components of the frequency spectrum to be underestimated, and the effect is more pronounced for the 256-point analog DFTs due to the much larger MVM size (512×1024). The 16-point analog DFTs have much lower summed currents on average due to the small MVM size (32×64), and hence has negligible IR drops. This is the main reason for the slightly larger PSNR for the SONOS-computed spectrogram compared to the 65,536-point FFT. For the largest outlier currents in Fig. 4b, the ADC clips the current measurement to the limit of 17 μA , leading to a negative error that increases linearly with the correct current value.

An analog FFT system can be dynamically re-configured to compute FFTs of smaller sizes without re-programming any memory devices. This cheap re-configurability is possible by exploiting a property of the DFT matrix. If N_1 is a multiple of N_2 , i.e. $N_2 = N_1/(a \times b)$ where a and b are positive integers, then it can be shown that: $(\omega_{N_2})^{nk} = (\omega_{N_1})^{na \times kb}$. Therefore, an N_2 -point DFT can be computed using a memory array that implements \mathbf{W}_{N_1} simply by applying the inputs to every a^{th} row and measuring the outputs from every b^{th} column. To demonstrate this, we down-sampled the audio waveform in Fig. 3a

by $16\times$ (to 4,096 points) and used the already programmed SONOS DFT-256 subarray to compute the FFT of the down-sampled signal, as illustrated in Fig. 4c. The SONOS-computed 4,096-point spectrum is shown in Fig. 4d, and has close agreement with the FP32 result (PSNR = 34.32 dB) wherever the signal exceeds the noise floor of the analog computation.

In addition to the audio waveform in Fig. 3a, we used the SONOS array to compute the spectrograms of eight one-second audio clips from the Speech Commands Dataset [41], using several different sizes of the elementary DFTs, up to and including the analog direct MVM (see Supplementary Information). In general, a larger elementary DFT size yields a logarithmically higher energy efficiency as explained earlier, but a smaller DFT size can potentially yield a higher accuracy due to reduced accumulation of conductance errors and parasitic IR drops (see Fig. 4b and Fig. S8). The optimal choice of DFT factorization is the one that maximizes efficiency while meeting the accuracy needs of the end application. For audio spectrograms, which are 2D visual representations of the audio, a realistic application is the identification of words and phrases using a convolutional neural network (CNN) [42, 43]. We show in the Supplementary Information that the SONOS-computed spectrograms are nearly ideal surrogates for FP32 spectrograms when passed into a CNN that was trained for voice command recognition.

5. Image processing using the analog vector-radix FFT

We now turn to image processing applications, which require the analog DFT approaches to be extended to two dimensions. The DFT of a two-dimensional $M\times N$ input \mathbf{x} can be computed with two matrix-matrix multiplications:

$$\mathbf{X} = [\mathbf{W}_N(\mathbf{W}_M\mathbf{x})^T]^T \quad (4)$$

Using resistive memory arrays, a direct computation of the above expression involves a sequence of N analog MVMs (M -point DFTs) followed by M analog MVMs (N -point DFTs). This will be called the analog direct MVM approach for the 2D DFT. Considering the case of $N\times N$ square-shaped 2D DFTs for simplicity, the energy of this approach scales poorly – $\mathcal{O}(N^3)$ – due to the need to partition the MVMs across many memory arrays when N is large.

By applying the Cooley-Tukey decomposition to both dimensions together, the computational complexity of the 2D DFT can be reduced dramatically. This multi-dimensional generalization of the Cooley-Tukey FFT is known as the vector-radix FFT (VR-FFT) [45, 46], and its mapping onto analog in-memory computing is illustrated in Fig. 5a for the 2D case. In this scheme, each dimension of the input is factored: $M = P\times R$ and $N = Q\times S$. The factors P , Q , R , and S are the sizes of the elementary analog DFTs, which are performed sequentially on the entire image in four stages with an element-wise twiddle multiplication step after the second stage. Alternatively, for very large images, these smaller DFTs can be recursively decomposed. The mathematical details of the analog VR-FFT are described in the Methods. If we again consider an $N\times N$ input, the energy of the analog 2D VR-FFT scales as $\mathcal{O}(N^2\log_K N)$, which is vastly more efficient than the analog direct MVM approach for large N , and is fundamentally similar to the $\mathcal{O}(N^2\log_2 N)$ energy scaling of digital FFT implementations in two dimensions [10].

We used the analog VR-FFT to experimentally compute the spectrum of spatial frequencies in 2D images, utilizing a SONOS subarray that is much smaller than the image size. We selected RGB exemplar images, shown in Fig. 5b, 5d, and 5e, that contain both satellite remote sensing imagery and natural scenes. For the VR-FFT, we decomposed each 256×256 image with the factors $P = Q = R = S = 16$, which allows all of the analog DFT steps to be computed by a single SONOS subarray programmed to the DFT-16 matrix. Fig. 5c shows the magnitude spectrum of the 2D spatial frequencies for the “Rotterdam” image as computed by the SONOS array, where each color channel of the image was processed independently. The magnitude is largest for low spatial frequencies near the center of the spectrum, and for spatial frequencies that lie along two diagonals that form a right angle. These correspond to the angles of the two perpendicular intersecting roads in the “Rotterdam” image.

To evaluate the fidelity of analog image processing, we used a digital FP32 IFFT to reconstruct the original image. We note that unlike prior experiments that tiled smaller reconstructions into a larger image [24], our reconstructions are based on the SONOS-computed frequency spectrum of entire 256×256 images. These are shown on the right side of Fig. 5b, 5d, and 5e for the three input images. To roughly compensate for signal loss caused by parasitic IR drops, the images were uniformly brightened using a correction factor based on Parseval’s theorem, as described in the Supplementary Information. In general, the SONOS VR-FFT preserves all of the spatial features in these images without introducing significant artifacts, though close inspection reveals a slight graininess caused by random analog conductance errors and circuit noise. We report in Fig. 5 two similarity metrics between the original and analog reconstructed image: the PSNR and the structural similarity (SSIM). Unlike the PSNR which is based on pixel-wise

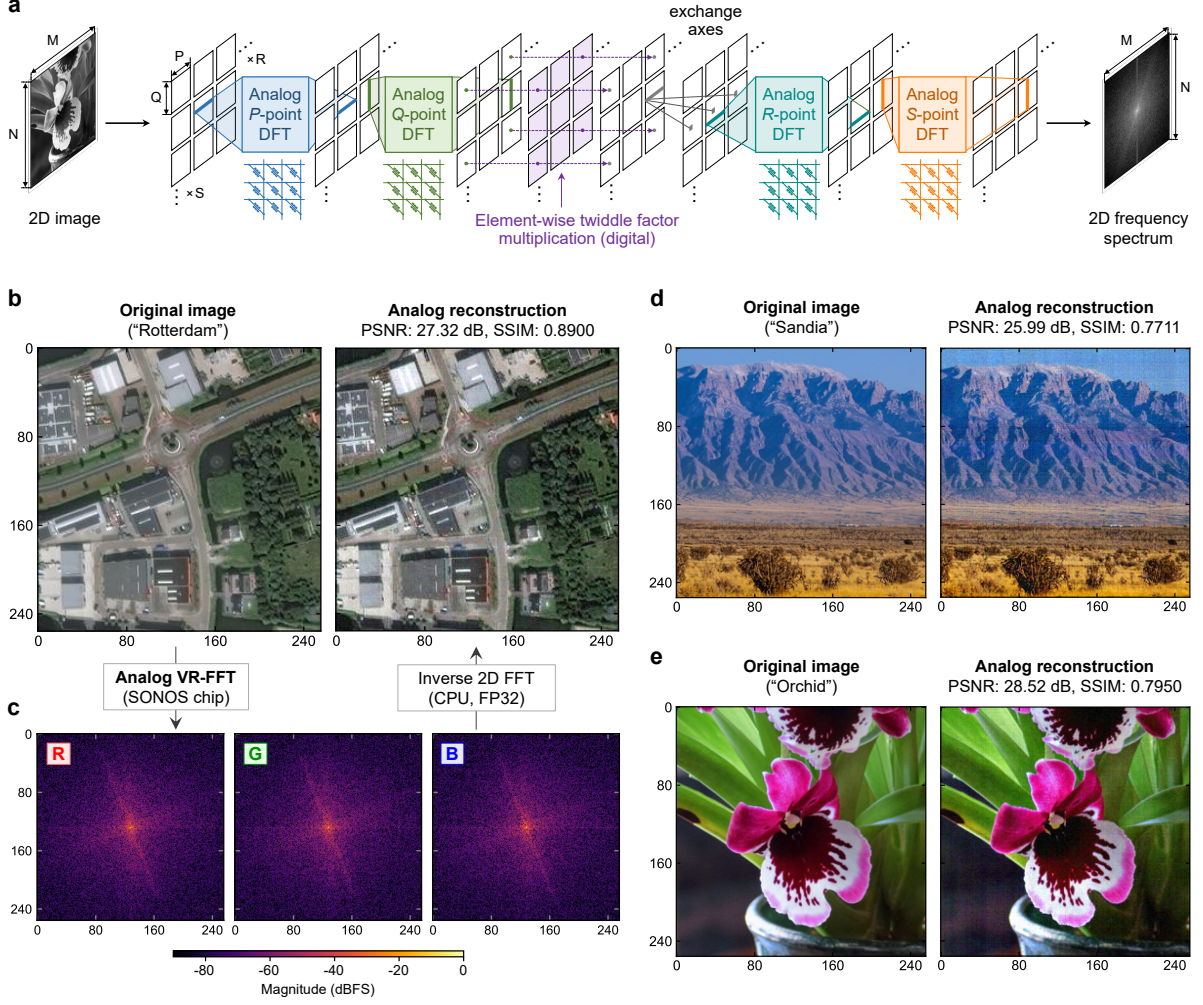


Fig. 5 Analog vector-radix FFT for 2D image processing. (a) Diagram of the analog 2D ($M \times N$) VR-FFT, which is composed of several analog DFT stages of smaller size. (b) Comparison of (left) a 256×256 input image with (right) the analog reconstruction of the same image. The input is a satellite overhead image of the city of Rotterdam from the SpaceNet-6 dataset [44]. The analog reconstruction is obtained by experimentally computing the analog VR-FFT of the image using the SONOS array (with $P = Q = R = S = 16$), followed by an ideal digital IFFT. (c) 2D magnitude spectrum for each color of the image in (b), computed using the SONOS array. (d-e), Original vs analog reconstruction for two other 256×256 images. (“Orchid” photograph was taken by the author. “Sandia” photograph from Dorothy Harris, Wikimedia Commons, CC-BY-2.0 license.)

differences, the SSIM measures statistical and structural differences between image variants [47]. All three reconstructed images have similarly high values of PSNR > 25 dB, but the SSIM has a greater variance, likely due to the metric’s sensitivity to the presence of high-contrast edges [48]. For practical image processing applications, the accuracy requirements on the analog FFT or DFT will depend on how the result is used by downstream algorithms or end users.

In addition to its superior scalability to the direct MVM method, the analog VR-FFT can also provide more numerically precise computation of the 2D DFT. To demonstrate this, we computed the DFT of the same 256×256 images by means of the analog direct MVM, using a SONOS subarray programmed to the DFT-256 matrix (512×1024 devices). Fig. 6a and 6b compare the reconstructed “Rotterdam” images formed from the 2D spectrum as experimentally computed by the analog VR-FFT and analog direct MVM, respectively. The direct MVM method produces significantly more degraded reconstructions with visible horizontal and vertical streaks, while the VR-FFT produced much cleaner reconstructions with higher PSNR and SSIM metrics. This is because the much larger array size of the 256-point analog DFT led to the use of a more compressed conductance range (0 to $1.7 \mu\text{S}$ vs. 0 to $20 \mu\text{S}$) to avoid saturating the ADC during MVMs, and therefore resulted in lower signal-to-noise ratio in the programmed SONOS weights. Despite the much lower conductances, the 256-point DFT was also more prone to the effects of parasitic IR drops due to larger summed currents. The analog computation of zero-frequency components

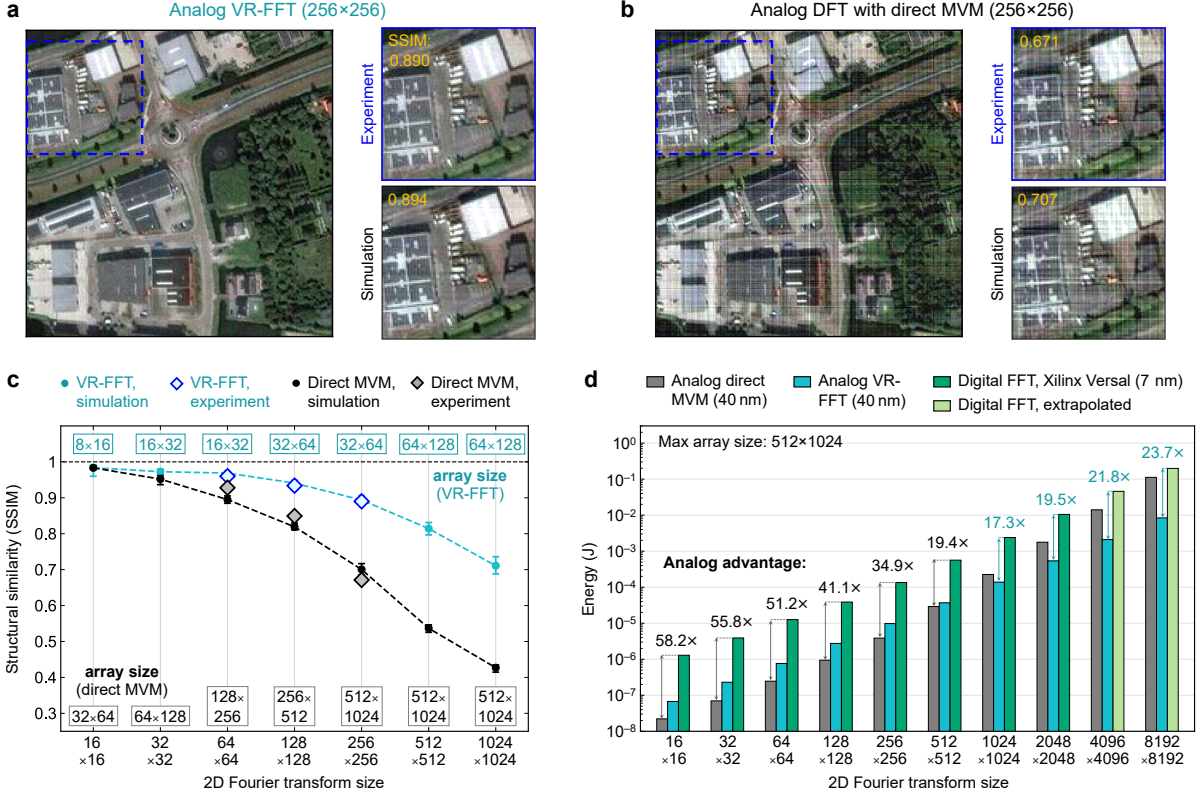


Fig. 6 Accuracy and energy scaling of analog Fourier transforms. (a) Left: experimental reconstruction of the Rotterdam image using the analog VR-FFT. Right: experimental and simulated reconstructions for a 96×96 cropped region. (b) Experimental and simulated analog reconstructions using analog DFTs implemented as direct MVMs. (c) SSIM of experimental and simulated analog reconstructions of the Rotterdam image at various sizes, using both the VR-FFT and direct MVMs. The input image was rescaled from a native resolution of 1024×1024 pixels. The top and bottom labels show the utilized SONOS array sizes for each data point, up to a maximum size of 512×1024 . The maximum SONOS conductance was scaled together with array size (see Methods). Error bars show the peak-to-peak variation in SSIM across ten Monte Carlo simulations. (d) Energy scaling of the 2D Fourier transform as computed by the analog direct MVM, analog VR-FFT, and the AMD Xilinx Versal chip. The analog energies assume a SONOS-based IMC accelerator in a 40-nm node. Versal performance is based on measurements up to an FFT size of 2048×2048 ; beyond this, the trend was extrapolated. The analog advantage is the ratio of the Versal’s energy to the lower of the two analog DFT methods.

along either dimension are particularly sensitive to these sources of error, leading to the streaks in Fig. 6b. Similar results for the two other 256×256 images can be found in the Supplementary Information.

To project how the accuracy scales with increasing image size, we simulated the analog reconstruction of the “Rotterdam” image at a variety of sizes, using both the analog VR-FFT and the direct MVM. The simulation, which is described in Methods, replicates the characterized properties of the SONOS devices, ADCs, and metal interconnects in our fabricated chip. Two simulated reconstructions are shown in Fig. 6a and 6b, showing that the simulation accurately captures the differences between the two methods both in terms of SSIM and the experimentally observed artifacts. Fig. 6c summarizes the quality of the reconstructions vs. image size. For this analysis, the utilized SONOS conductance range was optimally reduced with array size to balance the effects of ADC saturation, parasitic IR drops, and loss of weight precision (described in Methods). The analog direct MVM requires the largest array size possible to stay efficient, but as a result, it more quickly loses reconstruction fidelity at large image sizes for the reasons mentioned above. By comparison, the analog VR-FFT remains significantly more accurate at large image sizes by enabling the array size to scale much more slowly with the image size.

We have shown earlier that the analog FFT follows a fundamentally similar scaling law to the digital FFT: $\mathcal{O}(N \log N)$ in one dimension, and $\mathcal{O}(N^2 \log N)$ in two dimensions. A comparison of their actual energy consumption on problems of practical size requires knowledge of the missing constants of proportionality, which we now estimate using a combination of modeling and experimental benchmarking. Fig. 6d quantitatively compares the total energy of 2D DFTs of various sizes for the analog direct MVM, the analog VR-FFT, and the digital FFT. The energy of analog compute is modeled based on the maximum analog MVM size supported by our present SONOS array, but used peripheral circuits that are

different from those in our fabricated chip. These more optimal circuits were designed and simulated in the same 40-nm process, and assumed 8-bit inputs and 8-bit ADCs (see Methods). For the digital FFT, we compiled 2D FFT designs for the AMD Xilinx Versal, a state-of-the-art 7-nm chip that integrates a field-programmable gate array (FPGA) fabric with accelerators for machine learning and digital signal processing [49, 50]. The designs were executed on a physical Versal chip to measure throughput, and the designs’ power consumption was modeled using the Xilinx Power Design Manager (see Methods). Across all of the sizes shown in Fig. 6d, the more efficient analog solution has a $15\times$ to $60\times$ energy advantage over the digital FFT. Though the analog direct MVM is more efficient for small DFTs, the analog FFT is a necessary technique to realize analog hardware’s energy advantage for large problem sizes.

6. Conclusion

We have shown that the fast Fourier transform can be implemented on analog in-memory computing accelerators, enabling analog systems to efficiently scale to practically useful DFT sizes that were otherwise inaccessible. We used this approach to experimentally demonstrate a 65,536-point analog DFT computed using SONOS memory, which is more than three orders of magnitude larger than previous demonstrations [24, 26]. Notably, we have shown that by decoupling the DFT size from the physical array size, the analog FFT allows higher-accuracy DFTs to be computed while circumventing the analog errors that are accumulated in very large arrays. In digital systems, the FFT is a family of algorithms whose optimal implementation depends on the hardware [10]. Our results and analysis show that this is also true for analog FFTs, whose optimal radix and other implementation details depend on the size of the memory array, the available die area, and the desired accuracy, energy efficiency, and throughput of the computation. While analog FFT accelerators can use the same memory technology and in-memory computing circuits as analog ML accelerators, our analysis and experiments demonstrate that they will be optimized in different ways to perform these workloads accurately and efficiently. More broadly, the ability to map divide-and-conquer algorithms like the FFT greatly extends the scalability and versatility of low-power analog co-processors, potentially enabling new data processing capabilities that cannot be realized on today’s edge systems.

References

- [1] Walker, J. L. Range-doppler imaging of rotating objects. *IEEE Transactions on Aerospace and Electronic Systems* **AES-16**, 23–52 (1980).
- [2] Perry, R., DiPietro, R. & Fante, R. SAR imaging of moving targets. *IEEE Transactions on Aerospace and Electronic Systems* **35**, 188–200 (1999).
- [3] Richards, M. A. *et al.* *Fundamentals of Radar Signal Processing* Vol. 1 (McGraw-Hill New York, 2005).
- [4] Sun, S., Petropulu, A. P. & Poor, H. V. MIMO radar for advanced driver-assistance systems and autonomous driving: Advantages and challenges. *IEEE Signal Processing Magazine* **37**, 98–117 (2020).
- [5] Kates, J. M. Principles of digital dynamic-range compression. *Trends in Amplification* **9**, 45–76 (2005).
- [6] Launer, S., Zakis, J. A. & Moore, B. C. J. *Hearing Aid Signal Processing*, 93–130 (Springer International Publishing, Cham, 2016).
- [7] Hwang, T., Yang, C., Wu, G., Li, S. & Ye Li, G. OFDM and its wireless applications: A survey. *IEEE Transactions on Vehicular Technology* **58**, 1673–1694 (2009).
- [8] Cai, Y., Qin, Z., Cui, F., Li, G. Y. & McCann, J. A. Modulation and multiple access for 5g networks. *IEEE Communications Surveys & Tutorials* **20**, 629–646 (2018).
- [9] Michailow, N. *et al.* Generalized frequency division multiplexing for 5th generation cellular networks. *IEEE Transactions on Communications* **62**, 3045–3061 (2014).

- [10] Duhamel, P. & Vetterli, M. Fast Fourier transforms: A tutorial review and a state of the art. *Signal Processing* **19**, 259–299 (1990).
- [11] Hennessy, J. L. & Patterson, D. A. A new golden age for computer architecture. *Communications of the ACM* **62**, 48–60 (2019).
- [12] Burr, G. W. *et al.* Neuromorphic computing using non-volatile memory. *Advances in Physics: X* **2**, 89–124 (2017).
- [13] Xiao, T. P., Bennett, C. H., Feinberg, B., Agarwal, S. & Marinella, M. J. Analog architectures for neural network acceleration based on non-volatile memory. *Applied Physics Reviews* **7**, 031301 (2020).
- [14] Sebastian, A., Le Gallo, M., Khaddam-Aljameh, R. & Eleftheriou, E. Memory devices and applications for in-memory computing. *Nature Nanotechnology* **15**, 529–544 (2020).
- [15] Li, C. *et al.* Long short-term memory networks in memristor crossbar arrays. *Nature Machine Intelligence* **1**, 49–57 (2019).
- [16] Yao, P. *et al.* Fully hardware-implemented memristor convolutional neural network. *Nature* **577**, 641–646 (2020).
- [17] Xue, C.-X. *et al.* A CMOS-integrated compute-in-memory macro based on resistive random-access memory for AI edge devices. *Nature Electronics* **4**, 81–90 (2021).
- [18] Wan, W. *et al.* A compute-in-memory chip based on resistive random-access memory. *Nature* **608**, 504–512 (2022).
- [19] Huang, Y. *et al.* Memristor-based hardware accelerators for artificial intelligence. *Nature Reviews Electrical Engineering* 1–14 (2024).
- [20] Ambrogio, S. *et al.* An analog-AI chip for energy-efficient speech recognition and transcription. *Nature* **620**, 768–775 (2023).
- [21] Le Gallo, M. *et al.* A 64-core mixed-signal in-memory compute chip based on phase-change memory for deep neural network inference. *Nature Electronics* **6**, 680–693 (2023).
- [22] Fick, L., Skrzyniarz, S., Parikh, M., Henry, M. B. & Fick, D. Analog matrix processor for edge AI real-time video analytics. *IEEE International Solid-State Circuits Conference (ISSCC)* **65**, 260–262 (2022).
- [23] Cai, R., Ren, A., Wang, Y. & Yuan, B. Memristor-based discrete Fourier transform for improving performance and energy efficiency. *IEEE Computer Society Annual Symposium on VLSI (ISVLSI)* 643–648 (2016).
- [24] Li, C. *et al.* Analogue signal and image processing with large memristor crossbars. *Nature Electronics* **1**, 52–59 (2018).
- [25] Hu, M. *et al.* Memristor-based analog computation and neural network classification with a dot product engine. *Advanced Materials* **30**, 1705914 (2018).
- [26] Zhao, H. *et al.* Energy-efficient high-fidelity image reconstruction with memristor arrays for medical diagnosis. *Nature Communications* **14**, 2276 (2023).
- [27] Cooley, J. W. & Tukey, J. W. An algorithm for the machine calculation of complex Fourier series. *Mathematics of computation* **19**, 297–301 (1965).
- [28] Khaddam-Aljameh, R. *et al.* HERMES-Core — a 1.59-TOPS/mm² PCM on 14-nm CMOS in-memory compute core using 300-ps/LSB linearized CCO-based ADCs. *IEEE Journal of Solid-State Circuits* **57**, 1027–1038 (2022).

- [29] Yu, S., Jiang, H., Huang, S., Peng, X. & Lu, A. Compute-in-memory chips for deep learning: Recent trends and prospects. *IEEE Circuits and Systems Magazine* **21**, 31–56 (2021).
- [30] Aguirre, F. *et al.* Hardware implementation of memristor-based artificial neural networks. *Nature Communications* **15**, 1974 (2024).
- [31] Song, W. *et al.* Programming memristor arrays with arbitrarily high precision for analog computing. *Science* **383**, 903–910 (2024).
- [32] Xiao, T. P. *et al.* Analysis and mitigation of parasitic resistance effects for analog in-memory neural network acceleration. *Semiconductor Science and Technology* **36**, 114004 (2021).
- [33] Xiao, T. P. *et al.* On the accuracy of analog neural network inference accelerators. *IEEE Circuits and Systems Magazine* **22**, 26–48 (2022).
- [34] Burr, G. W. *et al.* Access devices for 3D crosspoint memory. *Journal of Vacuum Science & Technology B* **32**, 040802 (2014).
- [35] Agrawal, V. *et al.* In-memory computing array using 40nm multibit SONOS achieving 100 TOPS/W energy efficiency for deep neural network edge inference accelerators. *IEEE International Memory Workshop (IMW)* 1–4 (2020).
- [36] Xiao, T. P. *et al.* An accurate, error-tolerant, and energy-efficient neural network inference engine based on SONOS analog memory. *IEEE Transactions on Circuits and Systems I: Regular Papers* **69**, 1480–1493 (2022).
- [37] Agrawal, V. *et al.* Subthreshold operation of SONOS analog memory to enable accurate low-power neural network inference. *International Electron Devices Meeting (IEDM)* 21.7.1–21.7.4 (2022).
- [38] Koenig, W., Dunn, H. K. & Lacy, L. Y. The sound spectrograph. *The Journal of the Acoustical Society of America* **18**, 19–49 (1946).
- [39] Rashtchian, C., Young, P., Hodosh, M. & Hockenmaier, J. Collecting image annotations using Amazon’s Mechanical Turk. *NAACL HLT 2010 Workshop on Creating Speech and Language Data with Amazon’s Mechanical Turk* 139–147 (2010).
- [40] Baken, R. & Orlikoff, R. *Clinical Measurement of Speech and Voice* Speech Science (Singular Thomson Learning, 2000).
- [41] Warden, P. Speech commands: A dataset for limited-vocabulary speech recognition. *arXiv:1804.03209* (2018).
- [42] Abdel-Hamid, O. *et al.* Convolutional neural networks for speech recognition. *IEEE/ACM Transactions on Audio, Speech, and Language Processing* **22**, 1533–1545 (2014).
- [43] Piczak, K. J. Environmental sound classification with convolutional neural networks. *IEEE International Workshop on Machine Learning for Signal Processing (MLSP)* 1–6 (2015).
- [44] Shermeyer, J. *et al.* SpaceNet 6: Multi-sensor all weather mapping dataset. *IEEE/CVF Conference on Computer Vision and Pattern Recognition (CVPR) Workshops* (2020).
- [45] Rivard, G. Direct fast Fourier transform of bivariate functions. *IEEE Transactions on Acoustics, Speech, and Signal Processing* **25**, 250–252 (1977).
- [46] Harris, D., McClellan, J., Chan, D. & Schuessler, H. Vector radix fast Fourier transform. *IEEE International Conference on Acoustics, Speech, and Signal Processing* **2**, 548–551 (1977).
- [47] Wang, Z., Bovik, A., Sheikh, H. & Simoncelli, E. Image quality assessment: from error visibility to structural similarity. *IEEE Transactions on Image Processing* **13**, 600–612 (2004).
- [48] Nilsson, J. & Akenine-Möller, T. Understanding SSIM. *arXiv:2006.13846* (2020).

- [49] Gaide, B., Gaitonde, D., Ravishankar, C. & Bauer, T. Xilinx Adaptive Compute Acceleration Platform: Versal architecture. *ACM/SIGDA International Symposium on Field-Programmable Gate Arrays* 84–93 (2019).
- [50] Xilinx. Xilinx AI Engines and their applications, WP506 v1.2 (2023). URL: <https://docs.amd.com/v/u/en-US/wp506-ai-engine>.
- [51] Xiao, T. P., Bennett, C. H., Feinberg, B., Marinella, M. J. & Agarwal, S. CrossSim: Accuracy simulation of analog in-memory computing URL: <https://www.cross-sim.sandia.gov>.
- [52] Rasch, M. J. *et al.* Hardware-aware training for large-scale and diverse deep learning inference workloads using in-memory computing-based accelerators. *Nature Communications* **14**, 5282 (2023).
- [53] Xilinx. Versal 2D-FFT Implementation Using Vitis Acceleration Library Tutorial (XD073) (2023). URL: https://github.com/Xilinx/Vitis-Tutorials/tree/2023.2/AI_Engine_Development/AIE/Design_Tutorials/06-fft2d.AIEvsHLS/AIE.
- [54] Oppenheim, A., Willsky, A. & Nawab, S. *Signals & Systems* (Prentice Hall, 1997).
- [55] Bavandpour, M., Sahay, S., Mahmoodi, M. R. & Strukov, D. Efficient mixed-signal neurocomputing via successive integration and rescaling. *IEEE Transactions on Very Large Scale Integration (VLSI) Systems* **28**, 823–827 (2019).
- [56] Balasubramonian, R., Kahng, A. B., Muralimanohar, N., Shafiee, A. & Srinivas, V. CACTI 7: New tools for interconnect exploration in innovative off-chip memories. *ACM Transactions on Architecture and Code Optimization (TACO)* **14**, 14:1–14:25 (2017).
- [57] Horowitz, M. Computing’s energy problem (and what we can do about it). *IEEE International Solid-State Circuits Conference (ISSCC)* 10–14 (2014).

Methods

SONOS analog IMC demonstration system

The SONOS IMC chip used in this work was fabricated in a 40-nm node CMOS process at a commercial foundry. The formation of the SONOS memory cell in Fig. 2a was integrated into the front-end-of-line CMOS logic process. The IMC chip contains a 1024×1024 array of SONOS memory cells along with analog and digital circuitry to support write, read, and analog MVM operations. Fig. S2 shows the analog IMC demonstration system used in this work. The fabricated die was wire-bonded to a 100-pin thin quad flat package (TQFP), and the packaged SONOS IMC chip was mounted on a socket on a custom-designed circuit board. Commands and input/output data were sent to and from the IMC chip through an Infineon Technologies ARM microcontroller on a second custom-designed board. Four Keysight N6705C DC power supplies and a 9V power adapter were used to power the IMC chip, microcontroller, and boards. The microcontroller communicates with the host PC through a USB interface. All experiments were conducted through sequences of read, write, and analog MVM commands that were sent to the microcontroller using a Python application programming interface.

Programming and characterizing the SONOS array

The conductances of the SONOS devices were programmed with a write-verify algorithm that was designed to minimize variability and drift. To obtain precise and stable conductance values, the algorithm selectively places charge in deep, mid-gap electronic traps within the nitride that have a large energy barrier for charge confinement, while actively vacating charge from shallow traps near the band edges that can de-trap over short timescales [35, 36]. All of the conductances and currents reported in this work were measured with the same voltage bias at the four terminals of the SONOS cell in Fig. 2a: 0.06V on the bit line (V_{BL}), 2.5V on the select transistor gate (V_{SG}), 0V on the source line (V_{SL} , the select transistor source), and 0V on the control gate (V_{CG} , the SONOS transistor gate). This bias was also used for the verify operations during programming. The analog DFT operation also used the same biases, except that each select gate was switched between 0V and 2.5V depending on whether the applied bit of the corresponding input value was ‘0’ or ‘1’, respectively.

The state-dependent programming variability and conductance drift shown in Fig. 2c was characterized using an independent experiment that did not involve the DFT matrix; this is described in Supplementary Section S3. The resolution of the SONOS cell current measurements in Fig. 2d and Fig. 2e is 0.88 nA, set by the fine-resolution setting of the 12-bit ADC on the IMC chip. Additionally, Fig. S1c shows I - V curves of individual SONOS devices programmed to different states. These were separately measured using a semiconductor parameter analyzer to bypass the resolution limits of the on-chip ADC, and demonstrate that the device can be programmed to ultra-low conductances of ~ 10 pS ($>10^6$ conductance On/Off ratio), which we treat effectively as 0 μ S.

To program a DFT matrix, we use the scheme shown in Fig. 2b to map complex-valued matrix elements onto strictly real and positive conductances, which is similar to the method used in Refs. 23 and 26. The complex-valued matrix \mathbf{W}_K is first decomposed into four real matrices to support multiplication with a complex-valued input vector \mathbf{x} . Each real valued is encoded by the difference in conductance of two SONOS cells (positive and negative cell). We use the convention where for a positive-valued weight, the positive cell encodes the absolute value while the negative cell is programmed to a target of 0 μ S, and vice versa for negative weights [33]. The maximum conductance G_{\max} used for a given DFT array varies with the size of the matrix and the application (audio vs. image processing), as described later.

SONOS analog DFT computation

Input values are applied to the SONOS array in a bit-serial fashion to the select gate (SG) lines. If a bit is ‘1’, the SG is driven to 2.5V, the select transistor is ON, and the SONOS transistor conducts current from the BL to the source line (SL). If a bit is ‘0’, the SG is driven to 0V, the select transistor is OFF, and the cell does not conduct any current from the BL. Each BL is held at 0.06V by a voltage regulator. An individual MVM operation on the test chip was conducted between the stored DFT matrix and a binary slice of the input vector. The SONOS cell conducts current only in one direction (BL to SL), which keeps the conductance of the SONOS cell robust to small variations in the BL voltage. MVMs with positive and negative input values were computed in separate cycles then subtracted digitally. The summed current on each BL is converted to a voltage using a TIA, then converted to a 12-bit digital value by the ADC. For analog DFTs, we operated the on-chip ADC in a mode that has an input current dynamic range of 17 μ A and a current spacing between ADC levels of 4.88 nA. This wider range compared to the cell read operation accounts for the fact that the analog sum of currents during a DFT can be much larger than the current through a single SONOS cell. Any summed current that exceeds this current limit is clipped to the maximum value upon digital read-out.

To increase the throughput of the analog computation for smaller DFT sizes, we programmed multiple copies of the DFT matrix onto the SONOS array and tiled them block-diagonally. This allows the multiple binary slices of the input vector to be concatenated and processed simultaneously in a single analog MVM, rather than sequentially over multiple MVMs. All SONOS cells not lying along the block diagonal are programmed to 0 μ S. The large On/Off conductance ratio of the SONOS memory ensures that bit-wise MVMs computed in this manner remain independent. For DFT-16, we tiled the array four times ($N_{\text{tiles}} = 4$) to process four input magnitude bits at a time. We did not tile the DFT-64, DFT-128, or DFT-256 subarray ($N_{\text{tiles}} = 1$) due to their large size. In all, if the input \mathbf{x} is a vector of unsigned integers with N_{in} bits of precision, the number of analog MVMs used to compute a single DFT is $N_{\text{in}}/N_{\text{tiles}}$. If \mathbf{x} is a vector of signed integers, the number of analog MVMs is $2(N_{\text{in}} - 1)/N_{\text{tiles}}$. Each analog MVM involves a separate ADC operation. To obtain the full-precision, real and imaginary DFT outputs, the following digital post-processing steps were conducted at floating-point precision: (1) for each analog MVM, subtraction of the summed results for positive and negative weights, (2) for each input magnitude bit, subtraction of the results for positive and negative inputs, and (3) for each input magnitude bit, power-of-two weighted accumulation of the result.

For the input values to the analog DFTs, we used 13-bit signed integers (12 magnitude bits and a sign bit) for all audio and image processing experiments. The only exception was the input images to the first stage of the VR-FFT, where we used 8-bit unsigned integers since this was the original resolution of the JPEG images. Intermediate results between DFT stages were re-quantized to 13 bits prior to the next analog DFT stage, over a range that is set by the maximum value in the matrix of intermediate results. The digital baseline FFT used the same resolution for the input audio waveform or image as the analog computation, but used FP32 precision for the computation.

Twiddle factor multiplications between the DFT stages of the FFT were computed digitally at floating-point precision. Although not exploited in this paper, it is possible to fold the twiddle factor

multiplications into the analog DFTs, with some design trade-offs. This would allow the FFT to be computed entirely in analog, for cases where the Cooley-Tukey decomposition is not recursively applied. More details can be found in Supplementary Section S5.

The techniques described in this paper can be applied to efficiently compute large inverse FFTs (IFFTs) with analog in-memory computing, though this was not used in our experiments. For the analog IFFT, the conjugate transpose of the DFT matrix \mathbf{W}_N would be programmed onto the memory arrays to compute the elementary inverse DFTs.

Since the input audio or image signal for each of the experiments used in this paper was purely real, the frequency spectrum of the signal should be zero-symmetric, i.e. the spectrum should have equal components for positive frequencies and their corresponding negative frequencies along each axis. To produce the audio spectra in Fig. 3 and Fig. 4, we calculated the element-wise mean of the positive and negative frequency spectra computed by the SONOS array, then plotted the resulting magnitude spectrum. This averaging is why the spectrum shown in Fig. 4c of the 65,536-point analog FFT contains 32,768 points (0 to 8.000 kHz with a frequency bin spacing of 0.24414 Hz) even though the full spectrum originally computed by the SONOS array contains 65,536 points.

Vector-radix FFT details

We describe here the mathematical formulation of the 2D VR-FFT and its implementation in terms of analog MVMs, which is summarized in Fig. 5a. Analogous to the 1D case, the first step is to reshape the 2D input matrix \mathbf{x} to a 4D matrix $\tilde{\mathbf{x}}$, with dimensions $R \times S \times P \times Q$, where $M = P \times R$ and $N = Q \times S$. The values of R , S , P and Q are the sizes of the elementary DFT operations in the factorization and are directly related to the dimensions of the constituent analog MVMs. As drawn in Fig. 5a, this reshape can be visualized as partitioning \mathbf{x} into an $R \times S$ grid of sub-matrices, each of which has dimensions $P \times Q$. The matrix $\tilde{\mathbf{x}}$ has four indices: the pair (r, s) indexes a sub-matrix and the pair (p, q) indexes an element of the sub-matrix. In the VR-FFT, a $P \times Q$ 2D DFT is first performed on every sub-matrix $\tilde{\mathbf{x}}_{r,s}$, then the resulting matrix is element-wise multiplied by a matrix of twiddle factors $\mathbf{T}_{r,s}$ whose values also depend on the sub-matrix. The result is a 4D intermediate matrix \mathbf{y} with the same dimensions as $\tilde{\mathbf{x}}$, where each sub-matrix is specified by:

$$\mathbf{y}_{r,s} = \mathbf{T}_{r,s} \odot [\mathbf{W}_Q(\mathbf{W}_P \tilde{\mathbf{x}}_{r,s})^T]^T \quad (5)$$

Next, the positions of the (p, q) and (r, s) axis pairs of \mathbf{y} are exchanged to form a matrix $\tilde{\mathbf{y}}$ with dimensions $P \times Q \times R \times S$. Afterwards, an $R \times S$ 2D DFT is performed on every sub-matrix of $\tilde{\mathbf{y}}$:

$$\tilde{\mathbf{X}}_{p,q} = [\mathbf{W}_S(\mathbf{W}_R \tilde{\mathbf{y}}_{p,q})^T]^T \quad (6)$$

Finally, the 4D matrix $\tilde{\mathbf{X}}$ is re-shaped to obtain the 2D spectrum \mathbf{X} .

When implemented on analog hardware, each of the smaller 2D DFTs in Equation 5 and 6 is computed using a sequence of MVMs in a resistive memory array. Each of the four matrix-matrix multiplications in the two equations need to be performed to completion before starting the next step.

The number of ADC conversions needed for these analog MVMs, without any further application of Cooley-Tukey decomposition, is proportional to the product $PQRS$, or $\mathcal{O}(MN)$. In the limit of a very large 2D DFT where each of these four factors is also large, then these constituent 1D DFTs can be computed using 1D analog FFTs, and their energy would each scale as $\mathcal{O}(N \log_K N)$, where K is the size of the elementary analog DFT. The total number of ADC conversions needed for the VR-FFT would scale in this regime as $PQRS \times (\log_K P + \log_K Q + \log_K S + \log_K R)$, which is equivalent to $\mathcal{O}(MN \log_K(MN))$. For square DFTs where $M = N$, this scaling law simplifies to $\mathcal{O}(N^2 \log_K N)$.

Maximum conductance scaling with DFT size

The maximum SONOS conductance G_{\max} that was used for programming a specific DFT array was set primarily on the basis of the ADC input current limit of 17 μA . Since the voltage used for MVM is fixed at 0.06V, if G_{\max} is too large, many of the analog current sums during a DFT can be clipped by the ADC, which reduces the fidelity of the DFT. We reduced the value of G_{\max} with increasing DFT size since a larger number of SONOS cell currents are summed. At the same time, if G_{\max} is too small, the effective precision of the DFT weights is reduced because the conductance variability (shown in Fig. 2c) becomes a larger fraction of the utilized conductance range. To balance these considerations, we set the conductance range by simulating all of the elementary DFT operations for each of our analog FFT/DFT experiments prior to programming. We collected simulated statistics on the analog current sums, found

the largest value of G_{\max} which ensured that 99.99% of the analog sums were not clipped by the ADC, and programmed the DFT array using this G_{\max} value. Some outlier currents are still clipped by the ADC, which can be seen in Fig. 4b. Most of the clipping occurs on the less significant input bits which have a more balanced distribution of 0's and 1's compared to the higher bits, which generally have more 0's than 1's. Fortunately, the impact of clipping on the less significant bits is suppressed by the power-of-two weighted accumulation of the bit-wise MVM results.

The optimal value of G_{\max} also depends on the application. Different types of input signals have different value distributions, and these factors affect the distribution of analog current sums that arrive as inputs to the ADC. For example, the speech audio waveforms have a negligible component at zero frequency, while the opposite is true for the 2D images. For the audio processing experiments, we used $G_{\max} = 20.0 \mu\text{S}$ for the DFT-16 array and $G_{\max} = 6.17 \mu\text{S}$ for the DFT-256 array. For the image processing experiments, we used the same G_{\max} for DFT-16 but $G_{\max} = 1.67 \mu\text{S}$ for DFT-256. The conductances used for other DFT sizes for both sets of experiments is shown in Fig. S5a. For the image processing experiments, these G_{\max} values are also shown in Table 1.

Quality metrics

This work used the standard definition of the PSNR metric: $\text{PSNR} = 10 \cdot \log_{10} [S_{\max}^2 / \text{MSE}]$. Here, S_{\max} is the maximum single value in the ideal FP32 spectrum or image, and MSE is the mean squared error between the FP32 spectrum or image and the SONOS-computed spectrum or image reconstruction. The error is evaluated on a pixel-by-pixel basis and the mean is taken over all pixels. For structural similarity, we used the SSIM implementation in the scikit-image image processing library in Python, which is based on the implementation by Wang *et al* [47]. For this paper, all reconstructions of audio waveforms and images from SONOS-computed spectra were done using 1D or 2D IFFTs at FP32 resolution on a CPU.

Accuracy simulations of the SONOS FFT/DFT

The accuracy simulation results in Fig. 6a-c for the analog FFT and direct MVM were conducted using the CrossSim modeling tool [51]. The analog hardware parameters in CrossSim were chosen to provide a close match to the SONOS IMC chip, including: DFT matrix data mapping, range and resolution of conductance targets, SONOS cell variability, SONOS cell drift of three days, SONOS read noise, MVMs with bit-serial inputs, 12-bit ADC quantization and clipping, and parasitic resistances in the array. Modeling of the variability and drift in the SONOS cells after three days is based on the statistical data from the state characterization experiment, shown in Fig. S3e and S3f. Read noise modeling is based on measured SONOS noise properties that can be found in Ref. 35. Most of the analog DFTs shown in this paper were conducted within three days of programming the DFT matrix onto the SONOS array, so the simulated drift is expected to be a worst-case bound on the actual drift in these experiments. Random errors due to SONOS variability and drift were re-sampled by running multiple Monte Carlo simulations of the full FFT or DFT, while random cycle-to-cycle read noise was re-sampled on every simulated analog MVM. To model the effects of parasitic IR drops on accuracy, we used a simple model where the error on the summed current increases quadratically with the correct value of the summed current, similar to the method used in Ref. 52. This fits well to the average trend of the errors in Fig. 4b, but does not capture the variations around the average. These variations are due to the input data dependence and spatial non-uniformity of the IR drops, which are computationally very costly to model on large-scale problems with millions of analog MVMs [32].

SONOS accelerator energy projections

The fabricated 40-nm test chip used for our experiments was designed to demonstrate precise SONOS device programming and accurate analog MVMs, but was not optimized for high compute performance or power efficiency. Therefore, to obtain the energy values in Fig. 6d, we used projections that are based on the measured properties of the fabricated 40-nm SONOS arrays and modeled properties of more optimal peripheral circuits that were designed and simulated in the same 40-nm foundry process. These circuit designs are described in detail in Ref. 36 and are summarized in Supplementary Section S10.

The energy consumption of these circuit blocks is based on simulations in Cadence Spectre using transistors in a 40-nm process design kit. We used this model to compute the energy of analog 1D DFTs of various sizes up to 256 points, shown in Table 1. For very small DFTs, the energy is dominated by the circuit block that generates the ramp signal for all of the column ADCs. For large DFTs, the energy scales with the number of columns, due to the increasing overhead of the current sensing, integration,

Elementary DFT size	SONOS array size (rows \times columns)	Max conductance (for Rotterdam image example)	Modeled SONOS DFT energy
4	8×16	20.00 μS	0.234 nJ
8	16×32	20.00 μS	0.316 nJ
16	32×64	20.00 μS	0.483 nJ
32	64×128	10.00 μS	0.826 nJ
64	128×256	5.00 μS	1.543 nJ
128	256×512	2.67 μS	3.077 nJ
256	512×1024	1.67 μS	6.496 nJ

Table 1 Modeled properties of elementary analog DFTs on 40-nm SONOS MVM core.

and ADC circuitry. We composed these elementary DFT energies to estimate the total energy of DFTs based on large partitioned MVMs as well as analog VR-FFTs. For the VR-FFT, if N is a power of four we used $P = Q = R = S = \sqrt{N}$; otherwise, we used $P = R$ and $Q = S$ where P and Q are adjacent powers of two whose product is N .

Versal AI Engine benchmarking

In order to experimentally benchmark the energy efficiency of the analog FFT against state-of-the-art digital signal processing (DSP) hardware, we compiled and executed 2D-FFT designs of varying sizes on the AMD Xilinx Versal AI Engines. Despite its name, the Versal’s AI Engines have been optimized for both DSP and AI/ML applications [50]. We followed the documentation in Ref. 53 to build and run the 2D-FFT designs for the Versal. The design implements a 2D row-column FFT using AI Engines that separately process the row-wise 1D FFTs and column-wise 1D FFTs, along with a data mover kernel that communicates with the AI Engines using a 128-bit AXI4-Stream interface. The AI Engines run at 1.00 GHz and the interface runs at 312.5 MHz. Designs were compiled using the Xilinx Vitis AI tool (version 2023.1) for the Xilinx VCK190 board, which contains a 7-nm Versal AI Core (VC1902).

We compiled different designs by varying the following critical parameters. (1) Size: We ran 2D $N \times N$ FFTs with dimensions ranging from $N = 16$ to $N = 2048$. The latter was the largest design that could be supported by the available memory on the Versal’s AI Engine tiles. (2) Data type: We ran designs using both the CINT16 and CFLOAT complex data types. (3) Number of instances: We conducted experiments with one ($\times 1$) or five ($\times 5$) instances of the same design running in parallel on the VC1902 chip. More instances linearly increased throughput but sub-linearly increased the total power, improving the system-level energy efficiency (performance/Watt) [53].

For all dimensions shown in Fig. 6(d), we report results that used the most energy-efficient Versal implementation ($\times 5$ instances) and the data type whose precision was most similar to that of our SONOS array (CINT16). Each of the compiled programs was serially written to a bootable program image. These image files were written to SD cards using the BalenaEtcher tool, and then booted up on the VCK190 board one at a time to be executed and benchmarked. Once on board, individual build images were loaded within the PetaLinux environment; once mounted, the compiled graph can be executed within the Versal’s AI Engines. For each design, the average latency T_{avg} of the individual 2D FFT operations was extracted from runtime trace data using custom Python scripts, which measure the time-stamp differences between the relevant data streams of interest. Estimates of the power consumption were obtained by using the Xilinx Power Design Manager tool in a vector analysis mode, which uses switching data from detailed timing simulations of the 2D-FFT designs to produce accurate estimates of signal toggle rates and dynamic power consumption. To enable a fair comparison with the modeled energy of the SONOS analog FFTs, we used only the power consumed by the AI Engines (P_{AIE}) which perform the processing, rather than the reported power of the full system. The energy of a 2D FFT computed on the Versal is then given by $P_{\text{AIE}}/T_{\text{avg}}$, which is plotted in Fig. 6(d) at various sizes. For the two FFT sizes that are larger than 2048×2048 (colored light green), we estimated the energy consumption by extrapolating from the trend for smaller FFT sizes. Extrapolation was done by assuming an $\mathcal{O}(N^2 \log_2 N)$ scaling trend which fits well to the data from the Versal chip for $N \leq 2048$.

Acknowledgements

We thank A. Talin and W. Wahby for comments and feedback on the manuscript. This work was supported by the Laboratory-Directed Research and Development (LDRD) Programs at Sandia National Laboratories. This article has been authored by an employee of National Technology & Engineering Solutions of Sandia, LLC under Contract No. DE-NA0003525 with the U.S. Department of Energy

(DOE). The employee owns all right, title and interest in and to the article and is solely responsible for its contents. The United States Government retains and the publisher, by accepting the article for publication, acknowledges that the United States Government retains a non-exclusive, paid-up, irrevocable, world-wide license to publish or reproduce the published form of this article or allow others to do so, for United States Government purposes. The DOE will provide public access to these results of federally sponsored research in accordance with the DOE Public Access Plan <https://www.energy.gov/downloads/doe-public-access-plan>.

Supplementary Information

Appendix S1 Charge-trapping memory device

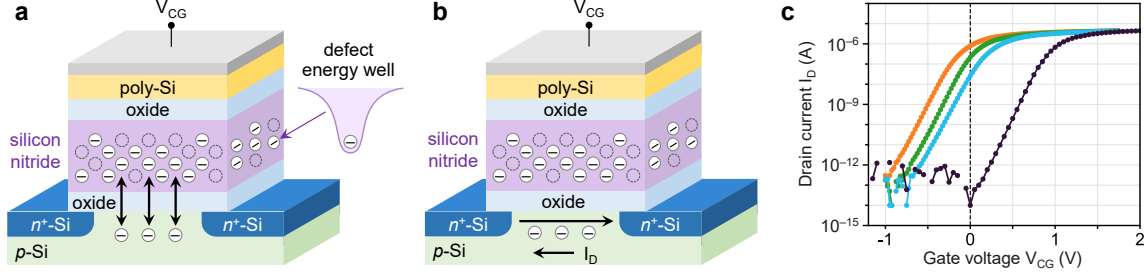


Fig. S1 Simplified diagram of a SONOS charge-trapping memory device. Relative dimensions of the layers are not to scale. (a) During programming, charge is injected into electronic traps in the silicon nitride layer via Fowler-Nordheim tunneling. (b) During read or analog MVM, current flows between the source and drain (left and right) terminals, through a channel whose conductance is electrostatically modulated by the trapped charge through the field effect. (c) I_D - V_{CG} transfer characteristics of a SONOS memory cell, which has four terminals as shown in Fig. 2(a). The curves correspond to four non-volatile states which draw a current of 800 nA (orange), 200 nA (green), 25 nA (blue), and < 1 pA (black) at $V_{CG} = 0$ V. Here, the select gate is fixed at 2.5V, the bit line voltage is 0.1V, and the select transistor source is 0V. Note that this bias differs from the bit line voltage of 0.06V used for reads and analog MVMs in the rest of the paper.

This work used a non-volatile charge-trapping memory technology based on the SONOS (silicon-oxide-nitride-oxide-silicon) material stack, shown in Fig. S1(a). The state variable in this memory is the quantity of charge that is stored within the silicon nitride layer, which is intentionally rich with defects that act as electronic trapping sites. During programming, charge is added or removed from the trapping layer by Fowler-Nordheim tunneling of electrons or holes through the lower oxide, as shown in Fig. S1(a). The amount of trapped charge changes the threshold voltage of the underlying transistor channel. The greater the number of trapped electrons in the nitride, the larger the gate voltage (V_{CG}) that is needed to form a conductive channel in the silicon layer below via the field effect, shown in Fig. S1(b). Therefore, while the stored charge is not part of the conductive channel, it electrostatically modulates the conductance of the channel. The quantity of charge within the structure remains stable over time due to the double confinement provided by the energy wells of the electronic traps, and the potential barriers at the nitride-oxide interfaces. The electronic traps span a range of energies inside the nitride bandgap; “deep” traps close to the midgap have larger energy barriers than “shallow” traps close to the band edges.

Fig. S1(c) shows the gate transfer characteristics of an individual SONOS cell, which also contains a select transistor and has four terminals, as shown in Fig. 2(a). The characteristics are shown for the same device when programmed to several different non-volatile states, indicating that the amount of stored charge shifts the threshold voltage of the channel. For this single-device measurement, we used a semiconductor parameter analyzer rather than the on-chip ADC. As described in Methods, during read and MVM operations, a fixed voltage bias ($V_{SG} = 2.5$ V, $V_{CG} = 0$ V, and $V_{BL} = 0.06$ V, relative to the select transistor source) is applied to the terminals, and the conductance of the SONOS device is defined under this operating bias. This condition is approximately represented by the dashed line in Fig. S1(c), with the difference that $V_{BL} = 0.1$ V in this measurement. Nonetheless, this shows that a very large dynamic range of conductance values spanning about six orders of magnitude is accessible.

A SONOS device that is programmed to operate in the subthreshold regime during a read or MVM can have extremely low conductances, as low as $G < 10^{-12}$ S; this state is used to store zero-valued DFT weights. For the non-zero DFT weights, we still primarily operate the SONOS device in the subthreshold region (or weak inversion regime) where the silicon channel has not fully inverted but its conductance can nonetheless be tuned with high precision. For the highest conductance values used in this paper ($G \sim 1$ μ S), we conduct the devices in the strong inversion regime, where an inversion layer with a high density of free electrons is induced in the silicon layer.

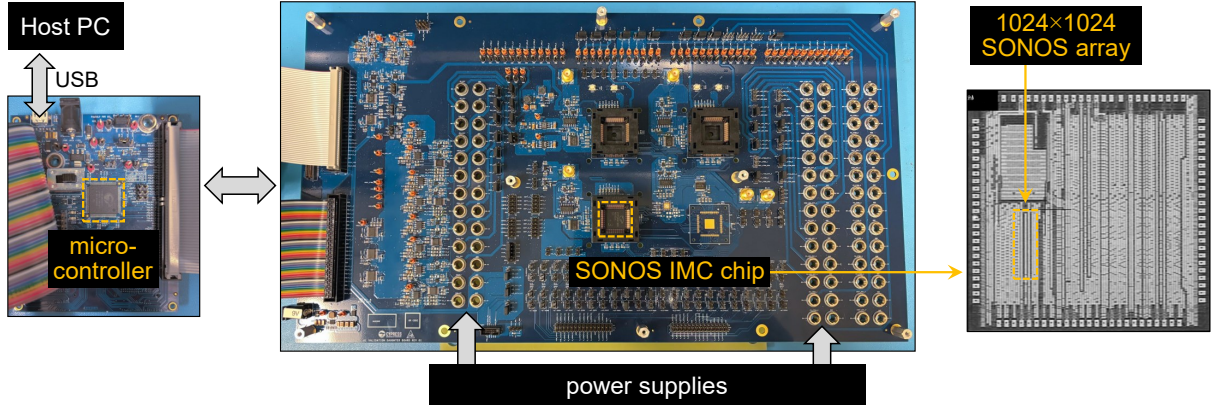


Fig. S2 Diagram of the hardware demonstration system used for the analog DFT and FFT experiments in this work. The packaged SONOS IMC chip was mounted on a 100-pin TQFP socket on a custom-designed board (center) that included components necessary to power the IMC chip. Only one of multiple sockets on the board was used for this experiment. Data and commands were sent to and from the IMC chip to an Infineon Technologies ARM microcontroller on a second custom board (left), connected to the center board through ribbon cables. The microcontroller communicated with the host PC through a USB interface. The boards were powered by four Keysight N6705C power supplies and a 9V power adapter, which were left disconnected in the photo. The right side shows a die photo of the IMC chip. The yellow rectangle shows the location of the 1024×1024 SONOS array, though the structure of the array is not visible due to metal over-layers.

Appendix S2 SONOS analog IMC chip and demonstration system

Fig. S2 shows the hardware demonstration system used for the experiments in this work. Additional details are described in Methods.

Appendix S3 Characterization of SONOS analog memory states

Prior to programming the DFT matrices used for the experiments in this work, we characterized the state-dependent conductance variability and drift characteristics of the SONOS analog memory cells. This was done by programming a 128×512 portion of the array to a gradient pattern of conductance targets. The gradient pattern consisted of a 4×32 tiling of 128 blocks, where each block is a 32×16 rectangular group of SONOS cells. All 512 cells within a block were programmed to the same current target. Across the blocks, 128 linearly spaced current targets were selected from 0 nA to 1400 nA (0 μ S to 23.3 μ S). Fig. S3(a) shows the measured conductances of all 65,536 SONOS cells in the gradient pattern just after programming. Fig. S3(b) shows a second measurement of the same cells taken three days after programming, where the effects of random charge leakage can be seen upon close inspection. The device conductances are derived from currents measured by the on-chip ADC. The ADC's current resolution is 0.88 nA and the devices are operated at a voltage of 0.06V, so the conductance resolution is 14.67 nS.

To better quantify the state dependence of these effects, we characterized the statistical properties of each of the 128 blocks of SONOS cells. Fig. S3(c) shows the distribution of SONOS conductances for 32 of the 128 blocks, measured just after programming. Because the target conductance is uniform within a block, the ideal width of each distribution is zero. The actual non-zero width of the distributions is due to random conductance variability in the SONOS cells caused by device-to-device process variation, write noise, and read noise. This variability directly causes random errors in the values of DFT weights used for analog computation.

In Fig. S3(c), the distributions asymptotically approach a width of zero in the limit of zero conductance. This is a unique property of the SONOS memory device when operated in the subthreshold conductance regime. In the subthreshold regime, the current through the SONOS transistor channel depends exponentially on the programmed threshold voltage V_T . The threshold voltage is approximately linearly related to the amount of stored charge in the nitride layer, and random variability in the quantity of charge translates linearly to a variability in V_T but exponentially to a variability in conductance. When the target conductance (or current) is very low, a large random variability in V_T may induce a large *relative* variability in the conductance, but a very small *absolute* variability due to the small conductance. It can be shown that in the subthreshold regime, the conductance variability is expected to be proportional

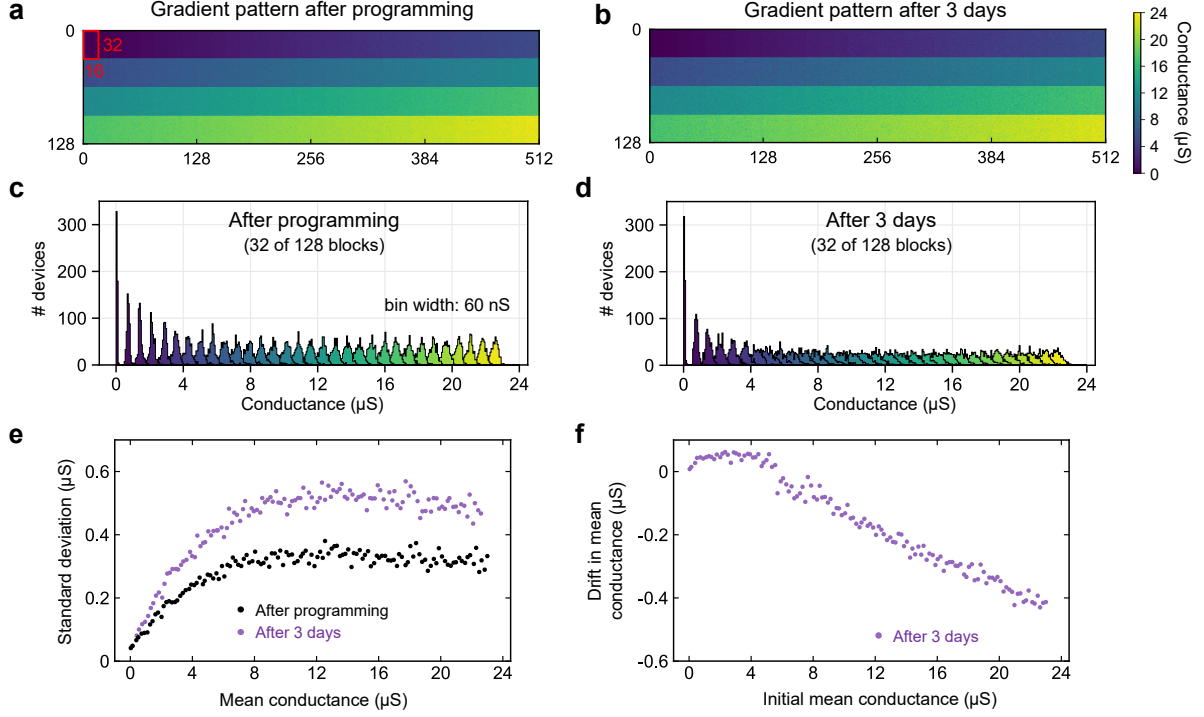


Fig. S3 (a) Spatial profile of measured SONOS conductances in a 128×512 sub-array that was programmed with a gradient pattern to characterized the state dependence of conductance variability and drift. Measurement was taken just after programming. A single block (out of 128) with a uniform target conductance is labeled. (b) Conductances in the same sub-array measured three days after programming. (c)-(d) Histograms of measured SONOS conductances in 32 of the 128 blocks (i.e. every fourth block) in (a) and (b), respectively. Each block is indicated by a unique color based on its target conductance and contains 512 devices. (e) Standard deviation of the conductance in all 128 blocks after programming and after three days; same as Fig. 2(c) in the main paper. (f) Drift in the mean conductance of all 128 blocks after three days, as a function of the initial mean conductance of each block.

to the conductance [36]; this explains the very narrow distributions in Fig. S3(c) as the conductance approaches zero. We quantify the width of a block's conductance distribution by its standard deviation, and this is plotted in Fig. S3(e) by the black points for all 128 blocks. The proportionality between conductance and variability at low conductance can be seen clearly. At larger conductances, the width of the distribution eventually saturates to the conductance tolerance used in the write-verify algorithm.

Fig. S3(d) shows the same distributions measured after three days. During this time, stored charge in the nitride layer can escape thermally from the electronic traps, and subsequently migrate to different locations in the nitride layer, or escape from the nitride layer through thermionic emission or tunneling through the oxide layers. The dynamics can be complex due to the presence of both trapped electrons and trapped holes, and the fact that a defect's influence on the channel conductance depends on its physical location within the nitride layer. The programming algorithm is designed to minimize de-trapping by selectively storing charge in deep traps near the middle of the silicon nitride bandgap, but a small number of carriers can nonetheless de-trap over this time period. The above effects induce a change in the channel's threshold voltage and conductance. Since these effects are thermal in origin and hence stochastic, the variability in conductance tends to increase over time. This causes the conductance distributions in Fig. S3(d) to be wider in general than the ones in Fig. S3(c). This can also be observed directly by comparing the black and purple points in Fig. S3(e).

We also observed that the conductance drift over time had some systematic state dependence. Fig. S3(f) shows how the mean conductance of each of the 128 blocks shifted over three days. Overall, the conductances tend to decrease with time indicating a net loss of holes or net gain of electrons over this time period. The state with the minimum conductance is the most stable with time for the same reason that it has the highest conductance precision; drift in V_T for deep subthreshold states induce a very small absolute change in conductance.

For the audio and image processing experiments in this paper, drift was an ongoing effect during the computation, i.e. later parts of the computation experienced more errors due to drift than the earlier parts. Nonetheless, a fixed drift time of three days represents a timescale that is longer than the worst-case

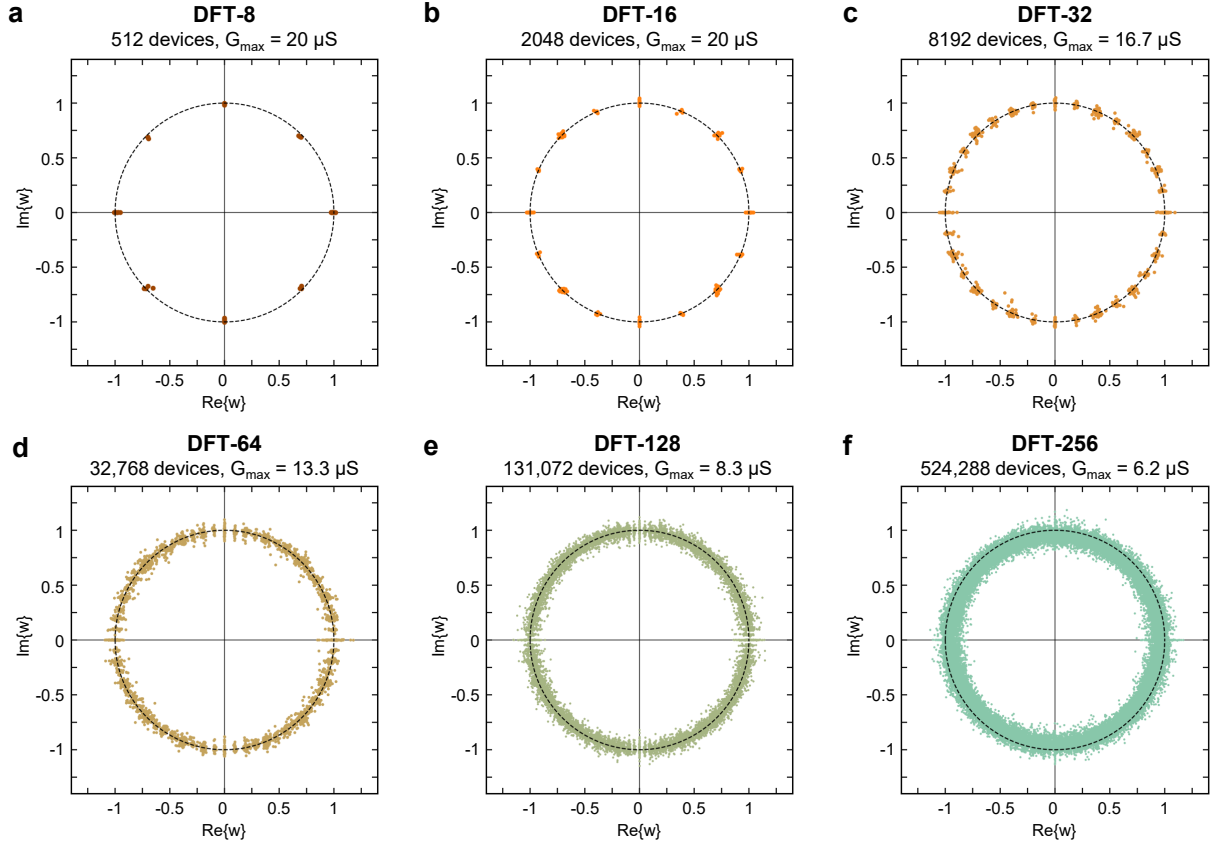


Fig. S4 Constellation of the complex-valued DFT weight values stored in the SONOS devices, for several sizes of the programmed DFT matrix. Weights are measured just after programming. The ideal DFT weights lie along the unit circle (dashed).

drift for many of the experiments, so for simulation purposes we used the three-day SONOS variability and mean drift characteristics in Fig. S3(e) and (f) and interpolated over conductance state. In general, the rate of conductance drift slows down with time as the loosely bound stored charge in the shallow traps of the silicon nitride are gradually depleted.

Appendix S4 Precision and distribution of DFT weights stored in SONOS devices

In addition to the DFT-16 and DFT-256 arrays shown in Fig. 2, we programmed DFT matrices of several other sizes onto the SONOS array. Fig. S4 shows the constellation in the complex plane of the DFT weights that are stored physically in the SONOS array for various DFT sizes. For all DFT matrices, the ideal weights have the form $\exp(-i2\pi nk/N)$ where n and k are the indices in the array. These complex exponentials all have a magnitude of 1, so the ideal weights all lie along the unit circle in the complex plane. For the smaller DFT matrices, only a few points along the circle are sampled. The weights stored in the SONOS devices are generally close to their target locations along the unit circle. Errors in the radial direction correspond to errors in magnitude, while errors along the circumferential direction correspond to errors in the phase of the complex-valued weights. Fig. S5(a) shows the mean absolute error (MAE) of both the magnitude (red) and phase (green) of the DFT weights for the different DFT sizes.

Since the DFT arrays in Fig. S4 were used to compute analog DFTs rather than used only for weight storage, we carefully chose the maximum SONOS conductance G_{\max} used to encode the DFT weights. Too large a value for G_{\max} induces errors due to large parasitic IR drops. Meanwhile, too small a conductance range reduces the effective precision of the stored DFT weights, because the conductance variability, noise, and drift become a larger proportion of the utilized conductance range. These considerations are described in Methods. Fig. S5(b) shows the chosen values of G_{\max} as a function of DFT size. These values were specifically chosen to optimize for the distribution of summed column currents for a given application; therefore, for some DFT sizes, two different values of G_{\max} were selected to process the speech audio

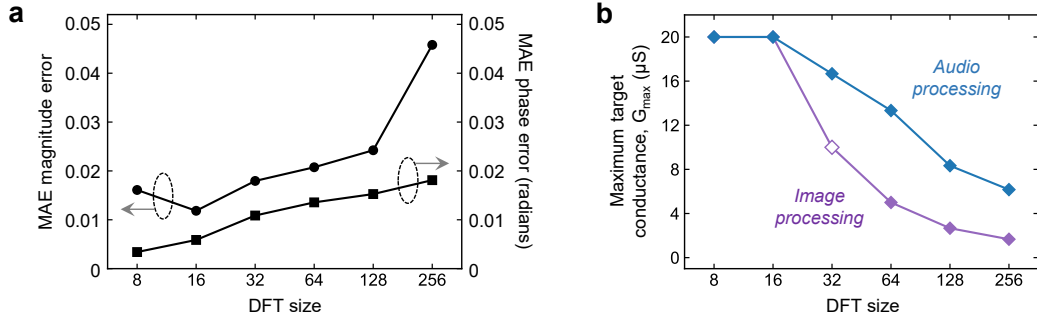


Fig. S5 (a) Mean absolute error in the magnitude and phase of the DFT weights stored in the SONOS array vs DFT size, based on the same SONOS weights in Fig. S4. (b) Maximum SONOS conductance used for storing the DFT matrix vs DFT size. For some DFT sizes, a different maximum conductance was used for the audio and 2D image processing experiments. The DFT-32 matrix was not used for any of the image processing experiments, though the selected value of G_{\max} was used for the simulations in Fig. 6(c).

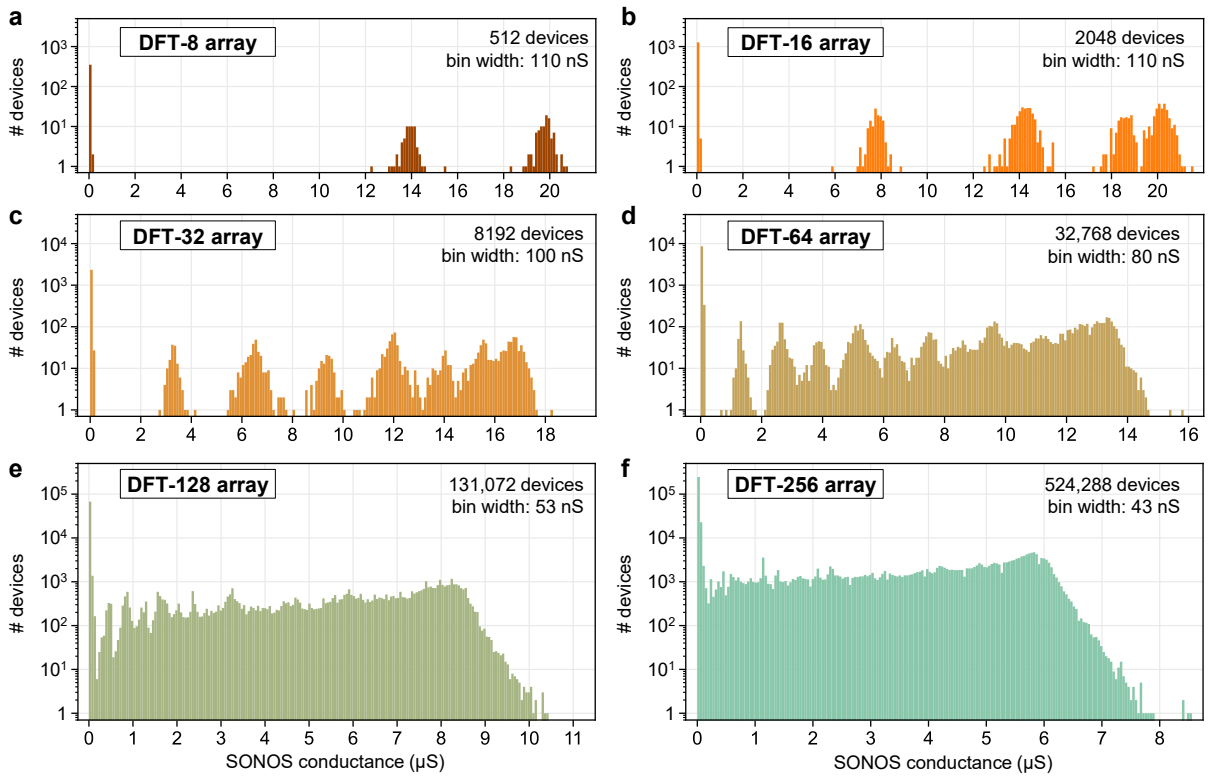


Fig. S6 Distribution of the measured SONOS conductance values corresponding to the programmed DFT matrices in Fig. S4. Conductances were measured just after programming.

waveforms (blue points) and the 2D spatial images (purple points), which have very different frequency spectra. For larger DFT sizes, which require larger arrays, the maximum conductance was reduced to keep the accumulated column currents low. At the level of individual DFT weights, because the range of SONOS conductances was reduced with increasing DFT size, both the magnitude and phase errors increase with DFT size, as shown in Fig. S5(a).

Fig. S5 shows the distributions of the individual SONOS conductance values used to implement the DFT matrices of different sizes in Fig. S4. As the size of the DFT increases, more values are sampled along the unit circles in the complex plane, causing a gradual transition from a more discrete distribution of values to a more continuous distribution. Each of the distributions contains a large peak at the minimum conductance, because our scheme for mapping positive and negative values implies that at least half of the SONOS devices in the array are programmed to the minimum conductance value. This scheme was chosen because it preserves the proportionality between the magnitude of a weight value and the conductance of the SONOS device [33].

DFT processing method	Energy scaling	Area scaling	Time scaling
Analog FFT	$\mathcal{O}(N \log_K N)$	$\mathcal{O}(N \log_K N)$	$\mathcal{O}(N \log_K N)$
Analog direct MVM	$\mathcal{O}(N^2/K)$	$\mathcal{O}(N^2)$ or $\mathcal{O}(N^2/K)^*$	$\mathcal{O}(\log_2(N/K))$
Digital FFT	$\mathcal{O}(N \log_2 N)$	–	$\mathcal{O}(N \log_2 N)$

Table S1 Asymptotic scaling laws for the energy, area, and time overheads of different DFT processing methods. *The area scaling depends on whether the memory elements or peripheral circuits dominate the area.

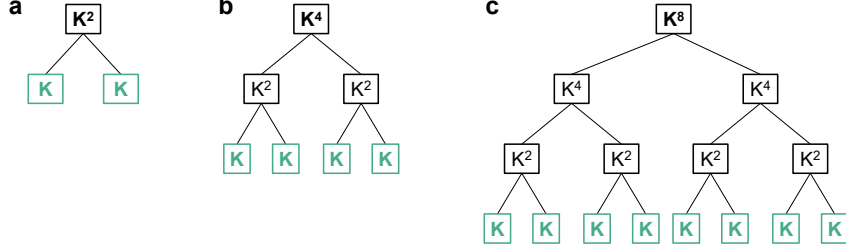


Fig. S7 Cooley-Tukey decompositions for three exemplary DFT sizes: (a) $N = K^2$, (b) $N = K^4$, and (c) $N = K^8$, where K is the largest analog DFT that can fit in a single resistive crossbar array.

There is a notable difference between the conductance distribution used for programming the DFT matrices, compared to the conductance distribution that results from programming neural network weight matrices. Across many different neural network models, it has been observed that the weight matrices tend to have a distribution of weight values that are heavily peaked around zero, with the number of weights decaying exponentially with increasing weight magnitude. When using our proportional differential mapping, this leads to conductance distributions that also decay exponentially away from the minimum conductance level [33, 36]. This is not the case for the DFT weights, especially if we ignore the many devices (at least 50%) that encode the negative magnitude of a positive weight, and vice versa. For the DFT matrix, because the complex-valued DFT weights are distributed uniformly around the unit circle, the conductance distribution is closer to uniform than exponential with a much higher average conductance value within the dynamic range of the device.

The above observation leads to an important difference in the error tolerance of the accuracy of analog FFTs with analog neural network inference. Analog neural network inference benefits enormously from having minimal error at the end of the conductance range of the device, while the error at the high end of the conductance range is less consequential [33]. Meanwhile, for analog FFTs, it is more important to keep the conductance errors low across the entire dynamic range of the device.

We note, however, that a higher precision in the minimum conductance level is still beneficial for analog FFTs when using a proportional differential mapping from weights to conductances, because half of the devices in the array will utilize the minimum conductance state.

Appendix S5 Scaling laws for energy, area, and performance of the analog FFT

In this section, we derive the mathematical scaling laws for the energy, area, and performance of the analog FFT and compare it with the analog direct MVM method and the digital FFT. We note that these are theoretical, asymptotic scaling laws and do not account for the actual costs of the underlying operations such as ADC conversions, digital multiplies, and memory accesses, which are dependent on the specific hardware implementation. These asymptotic scaling laws are also derived in the limit of large DFT size N ; the actual scaling behavior may not be a smooth function of N , and the scaling behavior can be different for small N , especially when $N \leq K$, where K is the largest analog DFT that can fit in a single resistive crossbar array. The analysis here considers only 1D DFTs, but can be straightforwardly generalized to two or more dimensions since higher-dimensional DFTs can be decomposed into 1D DFTs.

Table S1 summarizes the energy, area, and time scaling laws for the analog FFT, analog direct MVM, and digital FFT. We do not consider the area of the digital FFT in our analysis since it is highly dependent on the implementation. The explanations for these scaling laws are given below.

S5.1 Energy scaling of the analog FFT

To analyze the energy scaling properties, we will use the basic assumption from the main text that the energy of an analog MVM is dominated by the energy of the output peripheral circuits such as TIAs, integrators, and ADCs. This has been true for published analog IMC accelerators that use 8-bit or higher-resolution ADCs [13, 18, 28]. While neural networks can be trained to tolerate lower precision, we will assume that signal processing applications require at least 8-bit ADC outputs; this means 8 bits for the real output and 8 bits for the imaginary output of the DFT. Under the assumption that the peripheral circuits dominate the energy, the energy of an analog MVM scales with the number of output values. For the full analog FFT, we account for the energy of analog MVMs, the energy of digital twiddle multiplications, and the energy of reads and writes to digital buffers for intermediate data in the computation.

In order to compute the number of ADC conversions for an arbitrarily large N , we consider the three exemplary DFT sizes in Fig. S7. The $N = K^2$ case in Fig. S7(a) is the largest DFT that can be computed using only a single application of Cooley-Tukey decomposition. Following the procedure described in the main text, this involves K analog DFTs of size K , followed by another K analog DFTs of size K . Each analog DFT has $2K$ ADC conversions (for the real and imaginary outputs), so the total number of ADC conversions for the K^2 -point analog FFT is: $n_{\text{ADC}}(K^2) = K \cdot 2K + K \cdot 2K = 4K^2$. We now consider the $N = K^4$ case in Fig. S7(b), which is the largest DFT that can be computed using a Cooley-Tukey decomposition tree of depth ≤ 2 . At the top level, this DFT is factored into two sets of K^2 DFTs of size K^2 . Each K^2 -point DFT can be computed using the analog FFT in Fig. S7(a), so the total number of ADC conversions for this analog FFT is: $n_{\text{ADC}}(K^4) = 2 \cdot K^2 \cdot n_{\text{ADC}}(K^2) = 8K^4$. Carrying out this computation with one additional decomposition step, we can easily derive the total number of ADC conversions for the $N = K^8$ case in Fig. S7(c): $n_{\text{ADC}}(K^8) = 2 \cdot K^4 \cdot n_{\text{ADC}}(K^4) = 16K^8$. For the three cases in Fig. S7, the number of ADC conversions scales as $2N \cdot \log_K N$, and this $\mathcal{O}(N \log_K N)$ scaling law for the number of ADC conversions holds generally for increasing N .

The scaling law for the number of digital twiddle multiplications is similar to that for ADC conversions. In each Cooley-Tukey decomposition of a DFT of size N , the number of complex twiddle multiplications is N , applied to the intermediate results between the two DFT stages. Applying the same logic as above, the number of twiddle multiplications for the three cases in Fig. S7(a) are: K^2 , $3K^4$, and $7K^8$, respectively. The energy cost of the digital twiddle multiplications thus also scales as $\mathcal{O}(N \log_K N)$. Finally, because the ADC outputs and the twiddle multiplication outputs are the intermediate results in the analog FFT, the number of memory accesses associated with these buffered intermediate results also scales as $\mathcal{O}(N \log_K N)$. Therefore, because all major contributions to the energy of the analog FFT follow the same asymptotic scaling behavior, the energy of the analog FFT scales as $\mathcal{O}(N \log_K N)$.

S5.2 Area scaling of the analog FFT

We will consider the most compact implementation of the analog FFT, the elementary DFTs all have the same size, so that a single resistive memory array can be re-used for all of the analog portions of the computation. This may be the case if the lowest level Cooley-Tukey decomposition uses $N_1 = N_2$, or if N_1 is a multiple of N_2 as shown in the text. Even if multiple different sizes of the elementary DFTs are needed, the number of arrays would not be expected to scale with N .

The area associated with analog processing therefore depends on the area the resistive crossbar and peripheral circuits that implement a K -point analog DFT. If the array of memory elements dominates the area, then the area would scale as $\mathcal{O}(K^2)$. For highly scaled memory technologies, the area may instead be dominated by peripheral circuits, which would scale as $\mathcal{O}(K)$. Meanwhile, the area needed for intermediate digital storage scaled as $\mathcal{O}(N \log_K N)$, following the scaling of the number of intermediate results that need to be stored, as described above. Therefore, for large N , the area of the analog FFT system would be expected to scale as $\mathcal{O}(N \log_K N)$.

S5.3 Time scaling of the analog FFT

We previously determined that the number of ADC conversions scales as $\mathcal{O}(N \log_K N)$. In an analog MVM operation, all of the multiply-accumulate operations are processed in parallel across the full array, and we assume that the ADC conversions are also processed in parallel across the columns of the array. The latter can be accomplished using a ramp ADC as described in Methods. Under these assumptions, the latency of a single elementary analog DFT is $\mathcal{O}(1)$ and does not scale with K . Since each analog DFT is associated with $2K$ ADC conversions, this means that the time associated with analog MVMs scales

as $\mathcal{O}((N/K)\log_K N)$. Meanwhile, we assume that the time associated with the digital twiddle multiplications and digital memory accesses scale with the number of multiplications and accesses, respectively. Therefore, the time associated with both of these scale as $\mathcal{O}(N\log_K N)$, leading to an overall time scaling of $\mathcal{O}(N\log_K N)$ for large N .

In scenarios where the $\mathcal{O}((N/K)\log_K N)$ scaling of the analog MVMs limits the performance of the analog FFT, it is possible to trade off throughput with area. Taking the FFT in Fig. S7(a) as an example with $N_1 = N_2 = K$, the K DFTs of size K can be processed sequentially using a single array (as we have been assuming), or by K separate arrays in parallel that each store the DFT matrix \mathbf{W}_K . With the latter option, the time complexity of the analog FFT is reduced to $\mathcal{O}((N/K^2)\log_K N)$, but the area scaling of analog processing changes to $\mathcal{O}(K^3)$ if the memory array dominates, or $\mathcal{O}(K^2)$ if the peripheral circuits dominate. This may be a reasonable trade-off for small K where both the array size and the number of arrays can be kept relatively small. A benefit that comes “for free” with this more area-intensive approach is that the digital twiddle multiplications in the lowest-level Cooley-Tukey decomposition can be eliminated during runtime. This is done by extracting one column at a time of the $K \times K$ twiddle matrix \mathbf{T} and multiplying it element-wise with every column in \mathbf{W}_K , producing K unique matrices with the same size as \mathbf{W}_K . These matrices can then be programmed into the K resistive memory arrays for the second DFT stage of the Cooley-Tukey decomposition. This approach would increase the number of memory arrays from K to $2K$, since the arrays for the first and second stages of the decomposition would have different matrix elements. Applying this technique effectively folds the twiddle multiplications into the analog MVMs during runtime, increasing the energy efficiency. However, twiddle multiplications must still be implemented in digital for any higher-level Cooley-Tukey decompositions.

S5.4 Scaling laws for analog DFTs using direct MVMs

As explained in the main text, a direct MVM mapping of a DFT to analog IMC would require the DFT matrix to be split up across many arrays. In this case, K is proportional to the maximum dimension of a given array in this partition. The number of outputs for an N -point DFT scales as N , and each of these outputs must be obtained by digitally summing the partial results of N/K ADC conversions from different arrays. Therefore, the number of ADC conversions and the number of digital additions would both scale as $\mathcal{O}(N^2/K)$, and this is the overall energy scaling of the direct MVM approach.

Since the direct MVM approach stores every element of the matrix \mathbf{W}_N and does not require digital buffering, the area scaling is relatively straightforward. If the memory elements dominate the area of each array, the overall area scaling is $\mathcal{O}(N^2)$. If the peripheral circuits dominate the area, the overall area scaling is $\mathcal{O}(N^2/K)$. For the digital additions, we assume that enough adders are allocated so that partial results for each DFT output can be added in parallel to increase throughput. This would require $\mathcal{O}(N^2/K)$ digital adders.

In terms of performance, all of the analog MVMs across all of the arrays implementing the DFT can in principle be performed simultaneously, so the time complexity of the analog processing is $\mathcal{O}(1)$. Assuming as above that partial sums for different DFT outputs are added in parallel, the optimal throughput can be obtained by using an adder tree for each DFT output. This would lead to a time complexity of $\mathcal{O}(\log_2(N/K))$ for the partial result summations.

S5.5 Scaling laws for the digital FFT

The number of multiplications and the number of additions both scale as $\mathcal{O}(N\log_2 N)$ for all practical implementations of the FFT on digital hardware, such as the split-radix FFT, though the exact constants of proportionality and the lower-order scaling terms may depend on the exact implementation [10]. We assume that both the computation time and the energy consumption of digital FFTs increase proportionally with the number of arithmetic operations, so that both of these scale as $\mathcal{O}(N\log_2 N)$.

Appendix S6 Spectrogram generation with varying analog FFT factorizations

In addition to the audio caption in Fig. 3(a) with 65,356 samples, we also experimentally computed the spectrograms of eight audio clips containing spoken words from Google’s Speech Commands Dataset [41]. Most of these audio clips have 16,384 samples, for a duration of 1.024 seconds (16 kHz sampling rate). For each audio clip, different versions of the same spectrogram were computed using the SONOS analog IMC array with different factorizations of the DFT, including the analog direct MVM.

One of the waveforms, containing the word “stop”, is shown in Fig. S8(a). Fig. S8(b) shows the true spectrogram of this signal with a window size of 256 samples, computed using digital FFTs on a CPU at FP32 precision. Fig. S8(c) shows the same spectrogram generated experimentally using 256-point DFTs with analog direct MVMs on the SONOS array, using the DFT-256 subarray in Fig. 2(e). Finally, S8(d) shows the spectrogram generated using analog Cooley-Tukey FFTs, where each 256-point FFT was computed using 16-point DFTs on the SONOS array, i.e. $N_1 = N_2 = 16$. This computation was performed using the small DFT-16 subarray shown in Fig. 2(d). Both of the SONOS-computed spectrograms reproduce all of the key features of the FP32 spectrogram for the spoken word “stop”, including the initial high-frequency “s” sound and the louder, lower-frequency “top” sound. Similar to the experimental result in Fig. 3, the main visible difference between the FP32 and SONOS-computed spectrograms is the presence of the noise floor at around -70 dBFS that originates from random SONOS conductance variability and noise.

We also computed spectrograms for seven other voice commands and two other factorizations of the 256-point DFT. In sum, we computed spectrograms using four different factorizations: $(N_1 = 16, N_2 = 16)$; $(N_1 = 32, N_2 = 8)$; $(N_1 = 64, N_2 = 4)$; and 256-point analog DFTs implemented as direct analog MVMs. Fig. S8(e) summarizes how the DFT factorization affects the PSNR metric of the SONOS-computed spectrograms relative to the FP32 spectrogram. In general, the larger the size of the elementary analog DFT (based on the larger of the two factored DFTs), the lower the accuracy of the computation. As discussed in the main text, this is because the larger analog DFTs accumulate a greater amount of analog error from SONOS device conductance variations and noise, as well as accumulated parasitic IR drops along the array interconnects. The mean PSNR of the $(16, 16)$ and $(32, 8)$ factorizations are very similar. This may be due to the fact that while the 32-point analog DFTs have larger error on average than the 16-point analog DFTs, the slight difference is compensated by the 8-point analog DFTs, which have smaller error on average than the 16-point analog DFTs.

The trend in Fig. S8(e) illustrates the broader idea that the choice of factorization or radix used for the analog FFT can be used to trade off energy efficiency with accuracy. For the 256-point DFTs computed in Fig. S8, the most energy-efficient choice is the direct MVM, because the full DFT was computed by

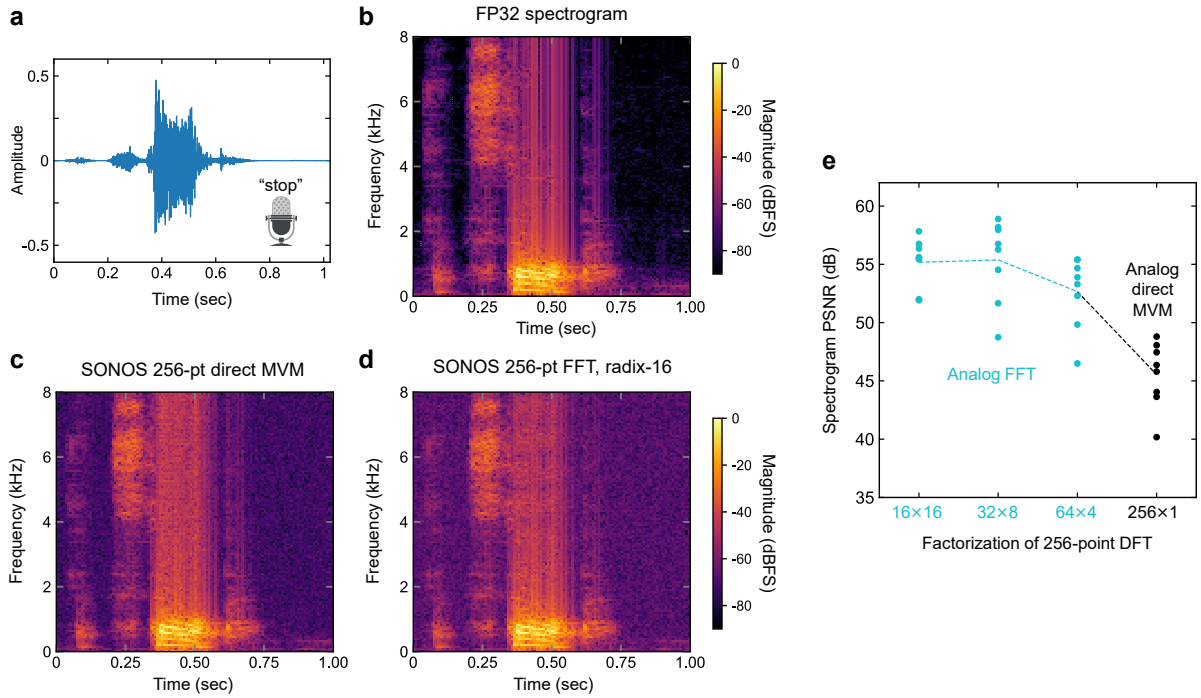


Fig. S8 (a) Audio waveform with 16,384 samples containing the spoken command “stop.” (b) Spectrogram of the audio waveform generated by FP32 FFTs, using a window size of 256 samples and a hop length of 128 samples. (c) Same spectrogram computed experimentally using 256-point analog DFTs implemented using direct MVMs on the SONOS array. (d) Same spectrogram computed using 256-point analog FFTs, factored into 16-point analog DFTs that are executed on the SONOS array. (e) PSNR of the SONOS-computed spectrogram relative to the FP32 spectrogram, for several DFT factorizations. For each factorization, eight spectrograms were generated for eight distinct command words. The dashed line connects the mean PSNR values across the commands. In order of increasing radix (left to right), the maximum SONOS conductances used are 20 μS , 16.7 μS , 13.3 μS , and 6.2 μS .

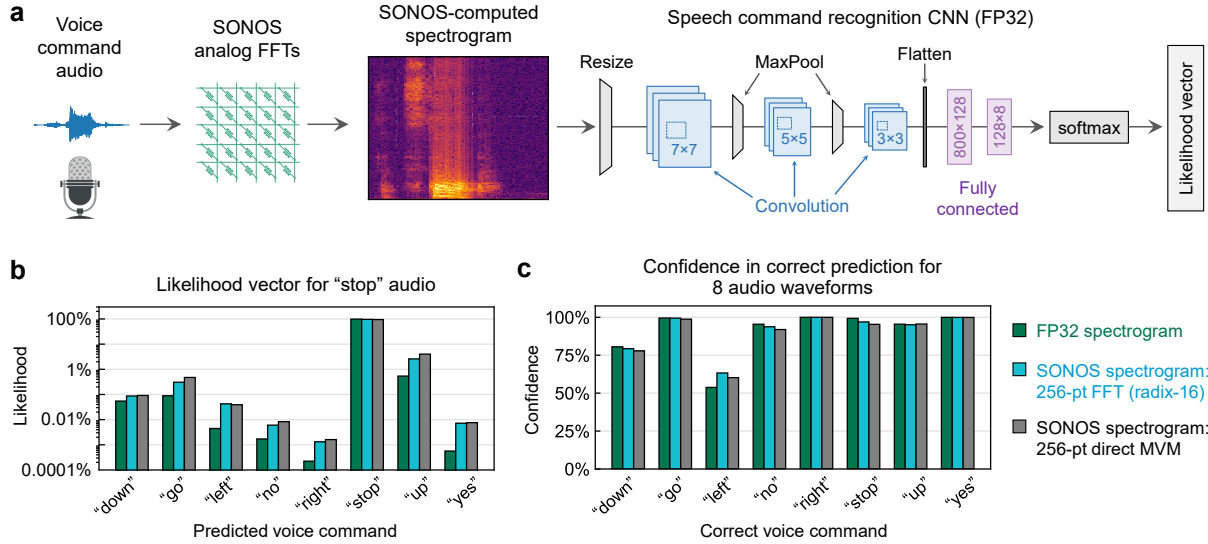


Fig. S9 (a) Structure of the CNN used to classify voice commands from spectrogram inputs. (b) Predicted voice command likelihood vector using the spectrograms in Fig. S8(b)-(d) as inputs, showing that all three spectrograms lead to a correct classification with similar likelihoods. (c) Confidence in the top predicted voice command for eight different input voice commands, using spectrograms that were computed using three different methods. Confidence is defined as the value of the largest element in the likelihood vector.

the SONOS array without having to split the DFT matrix. However, the option that yields the highest accuracy is the radix-16 FFT (i.e. $N_1 = N_2 = 16$) due to the smaller MVM size, even though it is about $2 \times$ less efficient based on Fig. 1(d). As mentioned in the main text, the optimal choice of DFT factorization is the one that maximizes energy efficiency while meeting the accuracy needs of the end application. For these voice commands, we further evaluate the quality of the SONOS-computed spectrograms by using them as input to a command recognition neural network. This is described in Supplementary Section S7.

Appendix S7 Voice command recognition from SONOS-computed spectrograms

To evaluate the impact of SONOS FFTs on downstream audio recognition tasks, a custom neural network was trained to classify distinct commands on a reduced version of Google’s Speech Commands dataset [41]. The dataset contains 8000 total waveforms for eight voice commands: “up”, “down”, “left”, “right”, “yes”, “no”, “stop”, and “go”. These audio files were split up into 6400 training examples, 800 validation examples, and 800 testing examples. We used a convolutional neural network (CNN), which is well suited for identifying spoken words from 2D features in audio spectrograms [42]. Prior to being passed into the CNN, ideal FP32 magnitude spectrograms were computed for all of the audio signals in the dataset, with a window size (FFT length) of 256 samples and a hop length of 128 samples, same as the examples shown in Fig. S8(b)-(d). The spectrograms were re-sized to 64×64 before the first convolution.

The CNN, whose architecture is shown in Fig. S9, contains about 140,000 weights across three convolutional layers and two fully-connected layers and was trained using the Tensorflow-Keras library. The neural network was trained for 10 epochs using the Adam optimizer with a learning rate of 10^{-3} and a batch size of 64. We used the sparse categorical cross-entropy loss function and included dropout layers before the penultimate and final layers of the network (at 25% and 50% dropout rates, respectively). The output of the neural network is a 1×8 likelihood vector, containing the estimated probabilities that the input signal belongs to each of the eight possible commands; the element with the highest likelihood is the predicted class. The trained network has a classification accuracy of 92% on the validation set, 91% on the training set, and 89% on the test set. To obtain a fair comparison between the SONOS-computed spectrograms and FP spectrograms, we ensured that the audio signals used in the SONOS experiment were not in the training set.

Fig. S9(b) shows the values in the likelihood vector, when each of the three spectrograms in Fig. S8(b)-(d) for the “stop” waveform in Fig. S8(a) are passed through the CNN. Not only is the correct command

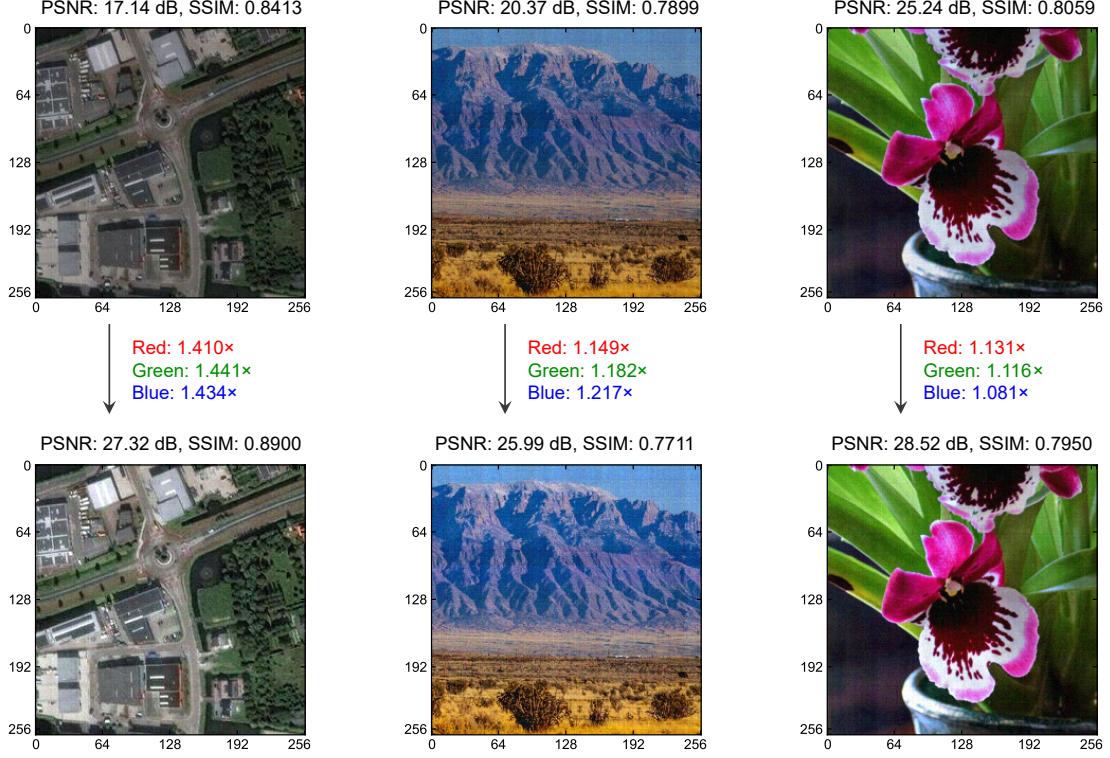


Fig. S10 (Top row) Uncorrected images reconstructed from 2D spectra computed by the SONOS array using analog VR-FFTs. (Bottom row) Reconstructed images after the channel-wise scalar correction.

(“stop”) predicted using all three spectrograms, all eight values of the likelihood vector are similar, indicating that using SONOS spectrograms (at both radix-16 and radix-256) yields nearly identical outcomes to using the FP32 spectrograms for recognizing this command.

Using SONOS-computed spectrograms in place of the FP32 spectrograms yielded the correct predicted class for all eight of the selected voice commands. Fig. S9(c) compares the confidence of these correct CNN predictions using different spectrograms, where we defined confidence as the predicted likelihood of the correct command. Both sets of SONOS-computed spectrograms yield nearly identical outputs from the CNN as the FP32 spectrograms, showing that the use of analog FFTs in this limited application can yield equivalent results to digital FFTs.

Appendix S8 Image correction using Parseval’s theorem

Parseval’s theorem states that the total energy of the signal is preserved through an ideal DFT [54]. For an $N \times N$ 2D DFT, this is expressed as:

$$\frac{1}{N^2} \sum_j \sum_k |X_{jk}|^2 = \sum_j \sum_k |x_{jk}|^2 \quad (\text{H1})$$

For an analog FFT or analog direct DFT, this does not exactly hold due to the presence of errors induced by the physical hardware. Specifically, the loss of stored charge from the SONOS device and the power dissipation in the parasitic resistances of the memory array cause a systematic loss of signal energy during the computation. For the 2D image reconstruction examples shown in Section 5, this signal loss has the effect of reducing the brightness of the reconstructed image.

We apply a first-order correction for this effect that takes advantage of Parseval’s theorem. The sums on the right and left side of Equation (H1) can be evaluated digitally before and after the analog Fourier transform computation, respectively. Then, we brighten the analog reconstructed image \mathbf{x}_R by multiplying every pixel by a scalar that depends only on the ratio of these two sums:

$$\mathbf{x}_{R, \text{corrected}} = \mathbf{x}_R \times \sqrt{\frac{\sum_j \sum_k |x_{jk}|^2}{\sum_j \sum_k |X_{jk}|^2 / N^2}} \quad (\text{H2})$$

We find that this brightening consistently improves the SSIM and PSNR of the reconstructed images. Nonetheless, since this is a simple scalar multiplication, all of the spatial features in the corrected image were already present in the uncorrected image. Therefore, the correction is unlikely to be necessary for applications that are not specifically optimizing for these metrics. We show images of the uncorrected analog reconstructions in Fig. S10.

Appendix S9 SONOS-computed 2D spectra and image reconstructions

Fig. S11, S12, and S13 show the full set of results from the 256×256 image processing experiments using analog VR-FFTs and DFTs implemented as direct MVMs. The 2D, complex-valued frequency spectra are the results that are computed directly using the SONOS array; only the magnitude spectra are shown for visualization purposes. The reconstructed images were generated by taking an FP32 inverse FFT of the complex-valued frequency spectra, then applying the correction described in Supplementary Section S8. All three of the original RGB images have a native resolution of 1024×1024 pixels or larger, and were re-scaled to a smaller size. We used SONOS arrays programmed with the DFT-16 and DFT-256 matrices for the VR-FFTs and direct MVMs, respectively. To program these matrices, we used the values of G_{\max} from Table 1 to set the conductance range, which is consistent with the simulations in Fig. 6(c).

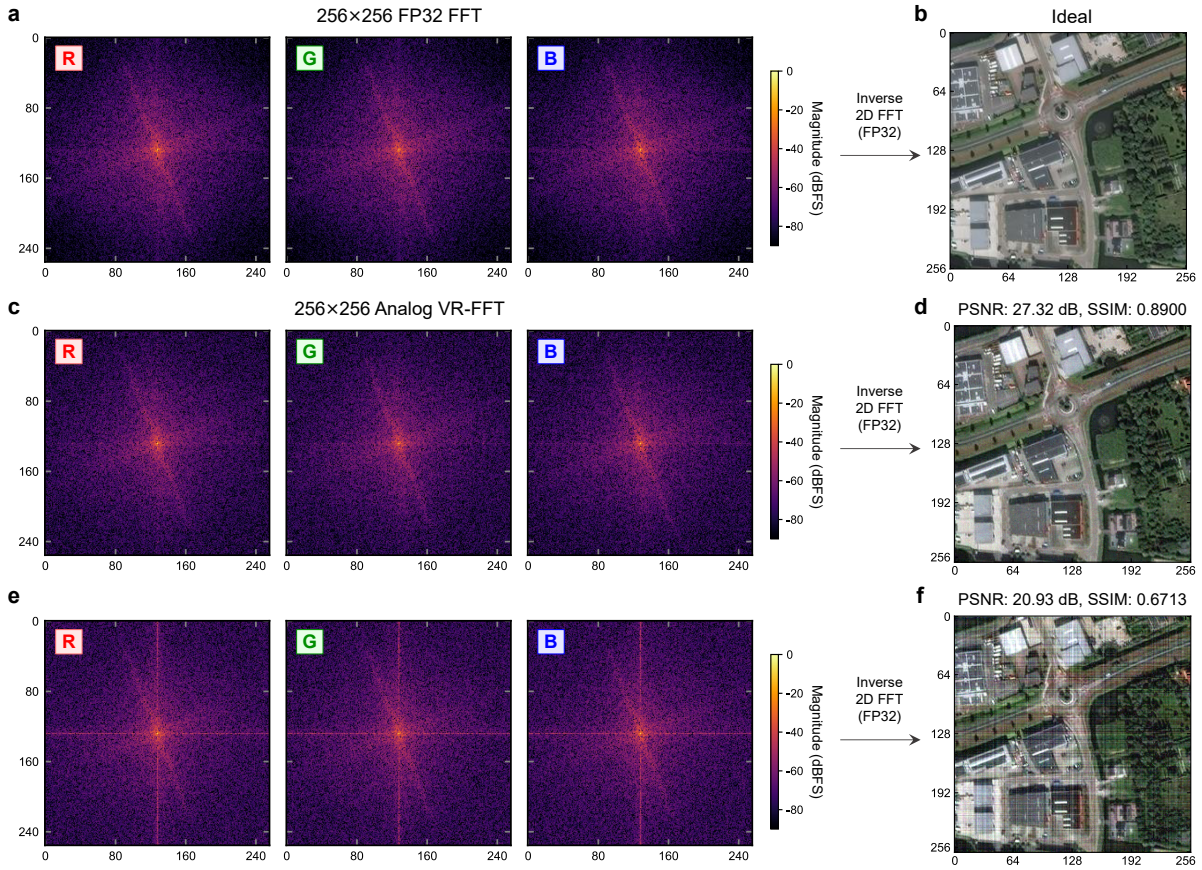


Fig. S11 (a) Ideal 2D magnitude spectrum of the 256×256 "Rotterdam" image computed using an FP32 FFT, shown for all three color channels. (b) The ideal reconstructed image, which is identical to the original image. (c) 2D magnitude spectrum computed by the SONOS array using the analog VR-FFT with $P = Q = R = S = 16$. (d) Reconstructed image from the spectrum in (c). (e) 2D magnitude spectrum computed by the SONOS array, with a 2D analog DFT implemented directly using MVMs. (f) Reconstructed image from the spectrum in (e).

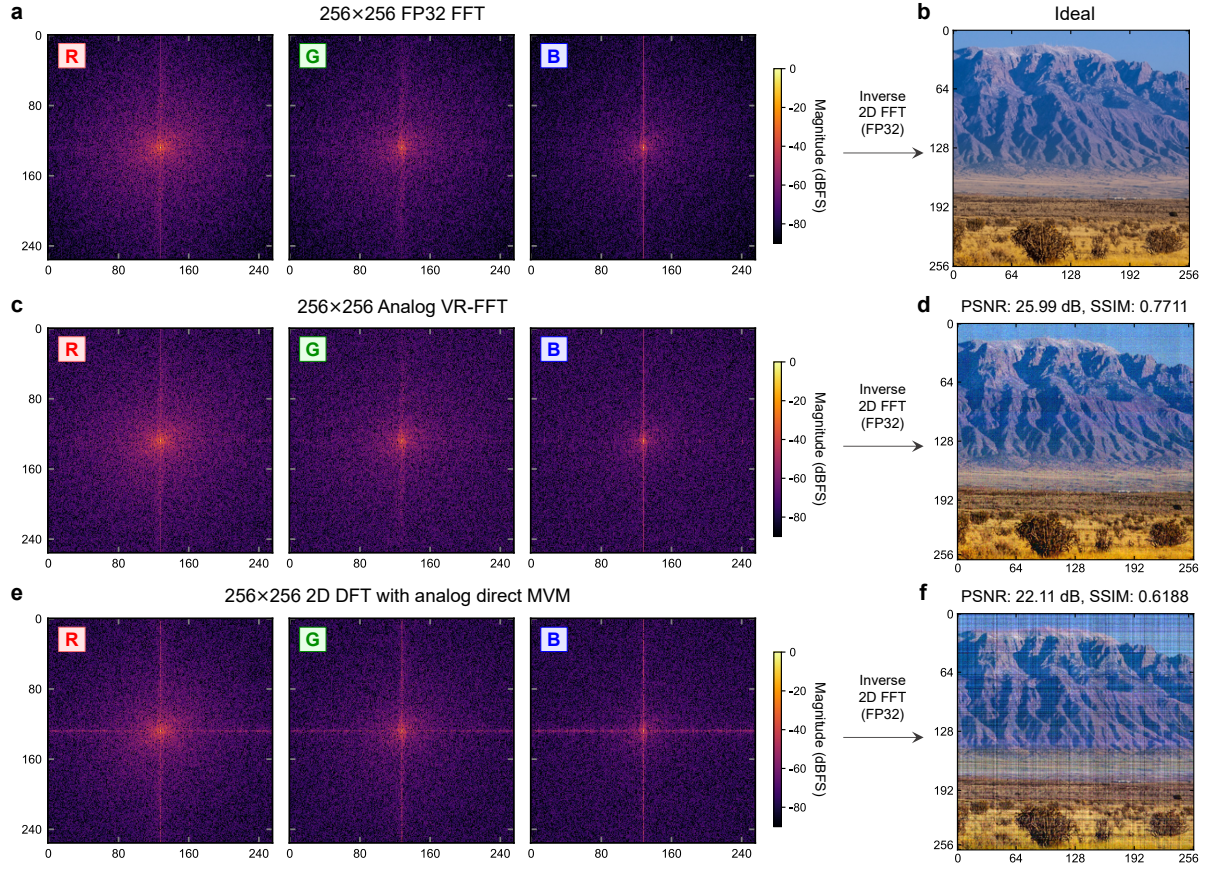


Fig. S12 (a) Ideal 2D magnitude spectrum of the 256×256 “Sandia” image computed using an FP32 FFT, shown for all three color channels. (b) The ideal reconstructed image, which is identical to the original image. (c) 2D magnitude spectrum computed by the SONOS array using the analog VR-FFT with $P = Q = R = S = 16$. (d) Reconstructed image from the spectrum in (c). (e) 2D magnitude spectrum computed by the SONOS array, with a 2D analog DFT implemented directly using MVMs. (f) Reconstructed image from the spectrum in (e).

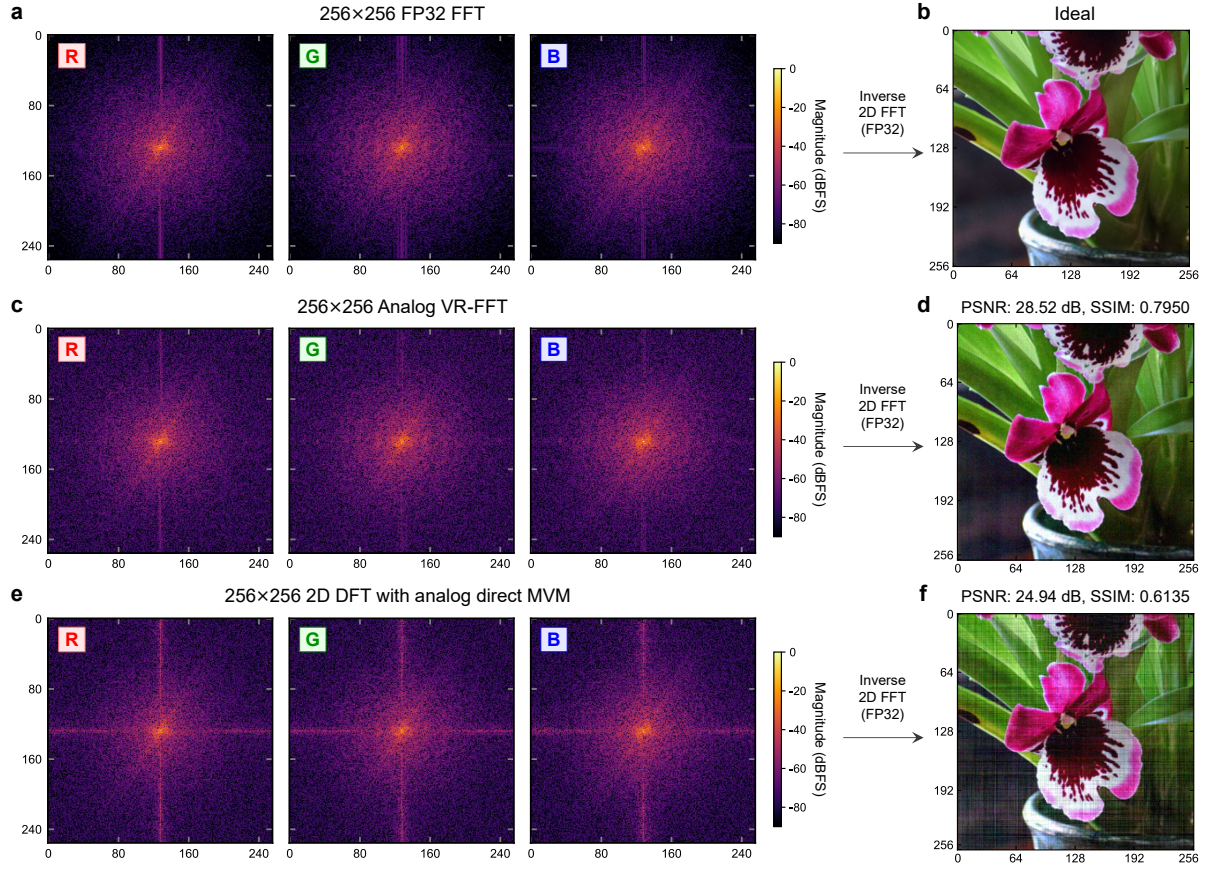


Fig. S13 (a) Ideal 2D magnitude spectrum of the 256×256 "Orchid" image computed using an FP32 FFT, shown for all three color channels. (b) The ideal reconstructed image, which is identical to the original image. (c) 2D magnitude spectrum computed by the SONOS array using the analog VR-FFT with $P = Q = R = S = 16$. (d) Reconstructed image from the spectrum in (c). (e) 2D magnitude spectrum computed by the SONOS array, with a 2D analog DFT implemented directly using MVMs. (f) Reconstructed image from the spectrum in (e).

Appendix S10 Details on SONOS accelerator energy projections

In this section, we provide additional details on the 40-nm circuit designs that were used to model the energy consumption of the analog DFTs. As described in the Methods, these designs differ from the actual circuits in the fabricated test chip, which was not optimized for power efficiency, but were simulated using a process design kit for the same 40-nm foundry process. These designs have been described in more detail elsewhere [36] and are summarized below.

The simulated design uses a SONOS-based analog MVM core that uses bit-serial application of digital inputs, same as our experiments, but the bit-wise dot products are accumulated in the analog domain rather than digital, by using a switched-capacitor circuit that implements the successive integration and rescaling technique [55]. This method reduces ADC energy consumption by using just a single ADC conversion for all input bits, rather than one conversion per input bit as in our test chip. We retain a differential conductance representation for signed weights, but use an offset subtraction scheme for signed inputs to allow positive and negative inputs to be handled in the same MVM. Positive and negative weight columns are connected to a pair of current conveyors with opposite current gain (+1 and -1) to allow analog subtraction of currents before the integrator, halving the required number of integrators and ADC conversions. We assume an ADC resolution of 8 bits for MVMs to reduce power consumption, different from the 12-bit ADC used in the fabricated test chip. A separate ADC resolution can be utilized for SONOS programming purposes. We use a ramp ADC design, where the integrated voltage on every column is compared (using a comparator) with a global voltage ramp signal; the staircase ramp is generated from a 1.0 GHz digital counter signal fed through a digital-to-analog converter (DAC) [36]. We assumed a streaming application where multiple SONOS arrays can compute different stages of the 2D DFT computation in parallel on multiple images; this allows one ramp generator to be shared by the ADCs of multiple SONOS arrays. For the analog direct MVM, two images can be pipelined over the two stages. For the analog VR-FFT, four images can be pipelined.

In addition to the analog MVM energies, we also estimated the cost of buffering the complex-valued digital intermediate results for 2D DFTs implemented using analog direct MVMs (two DFT stages) and VR-FFTs (four DFT stages). The real and imaginary components of each complex number are two separate 8-bit values. We used CACTI 7.0 [56] with a custom technology file for our 40-nm process to estimate the SRAM read and write energy, which sum to 3.48 pJ per 8-bit value. For the twiddle factor multiplication in the VR-FFT, we used an energy of 0.2 pJ per 8-bit integer multiplication, derived from energies for a similar 45 nm process [57]. This implies an energy of 0.8 pJ to multiply a complex-valued

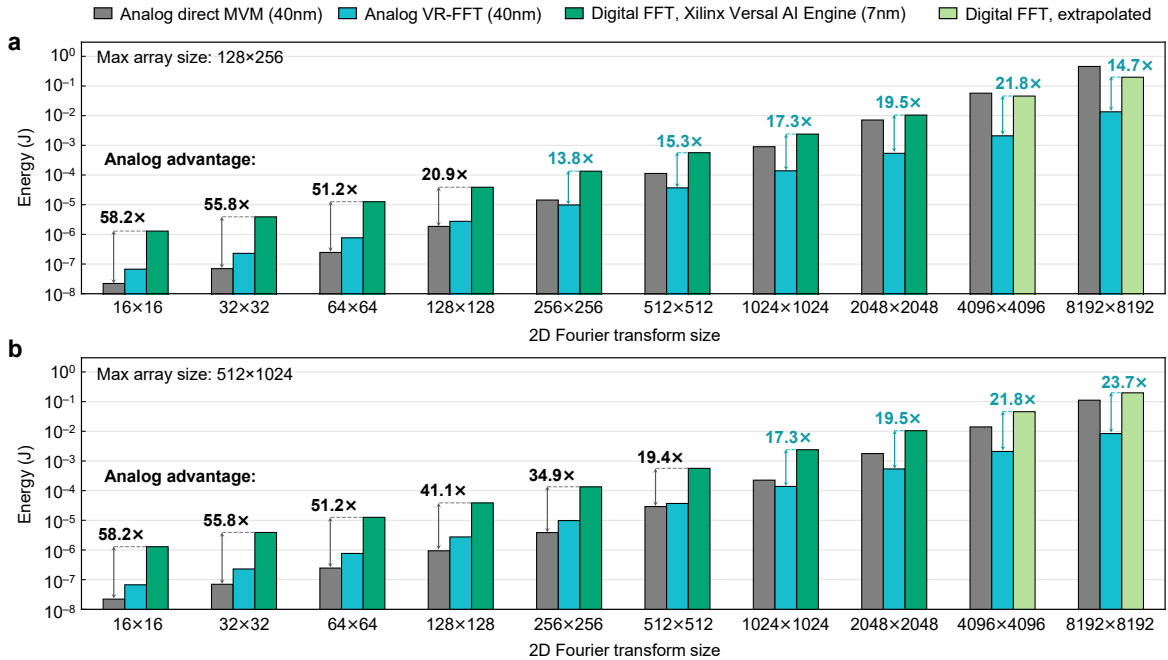


Fig. S14 (a) Energy scaling of the 2D Fourier transform as computed by the analog direct MVM, analog VR-FFT, and the AI Engine on the AMD Versal chip, assuming a maximum resistive memory array size of 128×256 . (b) Scaling characteristics, assuming a maximum resistive memory array size of 512×1024 . Reproduced from Fig. 6(c) for ease of comparison.

input with a complex-valued twiddle factor. The real and imaginary components of these products are re-quantized down to 8 bits prior to the analog DFT operations in the next stage.

Fig. S14(a) shows how the energy of 2D DFTs implemented using the analog direct MVM, analog VR-FFT, and digital FFT scale with the DFT size, for an array with dimensions 128×256 , which is large enough to fully store a DFT-64 matrix. The digital FFT energy values are the same as in Fig. 6(d), which is reproduced as Fig. S14(b) for ease of comparison. This array size is smaller than the SONOS array used in our experiments, and is closer in scale to some recently demonstrated ReRAM and PCM array prototypes [18, 21, 26, 31]. When using this smaller array size, the critical DFT size at which the analog FFT becomes the most efficient approach decreases. This is because implementing large DFTs with a direct MVM approach using the smaller array size requires the matrix to be partitioned across many more arrays, which is highly inefficient due to the rapid growth in ADC and peripheral circuit energy costs.